

Aftershocks of an Explosively Induced Mine Collapse at White Pine, Michigan

W. Scott Phillips¹, D. Craig Pearson¹, Xiaoning Yang¹ and Brian W. Stump²

¹Seismic Research Center,
Los Alamos National Laboratory
Los Alamos, New Mexico 87545, USA

²Department of Geological Sciences,
Southern Methodist University
Dallas, Texas 75275, USA

Bulletin of the Seismological Society of America
Submitted March, 1999
Revised July, 1999
LAUR 98-5694

ABSTRACT

We recorded an explosively induced, 320-m-deep, mine collapse and subsequent aftershocks at White Pine, Michigan, using an array of 12 seismic stations, sited within 1 km of surface ground zero. The collapse, which followed the rubblizing of a 2×10^4 m² panel of a room-and-pillar copper mine, was induced to facilitate leaching operations. The explosions produced little seismic energy; however, fracturing and collapse stages produced large signals that were observed at distances up to 900 km, yielding a magnitude (m_{bLg}) of 2.8. Previous work showed the initial collapse to be an expanding seismic source, interpreted as an opening tensile crack, opposite to the implosional character most often observed for natural mine collapses (Yang et al., 1998). We counted over 4000 aftershocks; their occurrence rate followed the modified Omori law: $\text{rate} = 560 \cdot (\text{time} - 0.01)^{-1.3}$, with time in hours. Based on P-wave polarities, we identified events of shear-slip, implosional and tensile character in the aftershock sequence. For shear-slip events, we found stress drops of 1 bar or less, seismic moments of 10^{15} to 10^{17} dyne-cm, (M_w -0.8 to 0.5) and source radii of 10 to 50 m. Corner frequencies for implosional events were relatively low, an indication that the collapsed cavity played a role in the source process. This caused implosional events to separate from other events in source parameter plots, providing a technique for classifying events of unknown type. We obtained locations of 135 aftershocks using P- and S-wave data. The aftershock zone was less than 100 m thick, situated just above and along the western, mined edge of the collapsed mine panel. Implosional events occurred at the bottom of the active volume, while shear-slip events were distributed throughout. Shear-slip focal mechanisms indicated thrusting along north-striking planes, consistent with the high, east-west regional compressive stress, coupled with a local decrease in vertical stress. The inferred deficit of vertical stress above the western panel edge following collapse indicated that overburden load shifted preferentially to the surrounding, un-mined areas, consistent with lower-than-predicted stresses measured in the first row of intact pillars.

INTRODUCTION

The 1995 controlled mine collapse at White Pine, Michigan gave us the opportunity to study a collapse-aftershock sequence in detail, by allowing advance deployment of a close-in seismic array. Our primary purpose was to study the seismic source, aiding our effort to discriminate between mine collapse, nuclear test and other man-made and natural seismic events, which will be important under the new Comprehensive Test Ban (U.N. General Assembly, 1996). However, ground motions generated by the collapse and associated aftershocks yielded a wealth of information pertinent to mine engineering and environmental issues as well. In particular, the distribution and failure modes of the aftershocks should be related to the induced stress changes (Hasegawa et al., 1989; McGarr, 1992a,b; Young and Maxwell, 1992; Urbancic et al., 1993; Baker and Young, 1997). Collapse-induced stress changes must be understood in order to predict the impact on surrounding mine structures, which will aid future design efforts to confine collapse to the planned area. Additionally, the distribution of aftershocks with depth may help evaluate any effect of the collapse on shallow layers where the local, potable aquifer resides. In the following, we will describe the collapse and aftershock data, analysis methods and results with emphasis on event classification, aftershock locations and source mechanisms, and discuss implications for stress redistribution and effect on mine infrastructure.

SETTING

The White Pine Mine is located near Lake Superior on the Upper Peninsula of Michigan (Figure 1). The primary mineral mined is copper, which was hydrothermally emplaced into low-grade, metamorphosed, sandstones and shales of pre-Cambrian age (Mauk et al., 1992). The underground workings at the mine, shown in map view in Figure 2, are extensive, with area of roughly 50 km². Historically, portions of the mine have collapsed "naturally." North-central portions of the mine have collapsed slowly over a period of many years. An area to the southwest of the White Pine fault failed catastrophically January 14, 1988, producing locally felt ground motions (M_L 3.6) and extensive damage to underground mine structures.

Room-and-pillar mining has been the primary ore recovery method at White Pine. Recently, a number of economic factors led to discontinuing the room-and-pillar operation and to investigating the effectiveness of pillar rubblization and in-situ leaching of the ore body remaining in the pillars. The controlled collapse documented here occurred in September 1995, and is the first of two collapse experiments performed at White Pine.

A layer of glacial till, 10 to 20 m thick covers the surface at White Pine. The top of the water table is shallow, 1-2 m beneath the surface. Pre-Cambrian bedrock, consisting of Freda sandstone, Nonsuch shale and Copper Harbor conglomerate, underlies the glacial till. The mine follows the shale-conglomerate interface at a depth of 320 m in our study area. The depth to this interface varies laterally. The White Pine fault strikes northwest-southeast (Figure 2) and dips steeply to the southwest. The fault bisects an anticlinal structure that plunges 10° to the southeast. These geological structures will be important to consider when calibrating the subsurface for microearthquake location purposes and for understanding the seismic response of different layers to collapse-induced stresses.

SEISMIC DATA COLLECTION

Prior to the collapse, we fielded a three-component, surface seismic network above the to-be-collapsed mine panel (Figure 3). Each station was instrumented with a six-channel, Refraction Technology Model 72A-08 data logger which was continuously locked to GPS-broadcast timing signals. Three-component, 1 Hz Mark Products Model L4-3C geophones were fielded at all stations and an additional three-component Terra Tech SSA-302 force-balance accelerometer was fielded at station 2. Sensors were deployed with horizontal components aligned to true north and east. Stations were programmed to record event-triggered data independently with the exception of station 13 (surface ground zero) which recorded in continuous mode. Stations 2 and 13 were digitized at 250 samples/s, other stations at 500 samples/s. Anti-alias filters were set with corners 95% of the Nyquist. Precise station locations were obtained using handheld GPS receivers (Table 1).

THE 1995 INDUCED COLLAPSE

The pillar-removal operation was conducted on September 3, 1995 at 5:39 PM local time (246:21:39:38 UTM). Ground zero was at 46.7297°N and 89.5012°W , the location of station 13. Seventy-two pillars with average dimensions of 6.1 m by 12.2 m were loaded with an average of 800 kg (1,800 lb.) of explosive per pillar for a total explosive source of 58,000 kg (130,000 lb.). A delayed firing pattern, 325 milliseconds in length, was used to minimize vibration effects at the surface and propagate the collapse toward the un-mined faces (Figure 4). The area of the collapsed panel was roughly $2 \times 10^4 \text{ m}^2$.

All seismic stations triggered on the induced collapse event and continued to trigger during the aftershock sequence. Because there was no noticeable expression of the collapse at the assembly point, 5 km from ground zero, a video camera deployed near surface ground zero was

recovered within 1 hour of collapse to verify that the explosives had detonated and the collapse had occurred. During recovery of the camera, aftershocks could be felt and heard at surface ground zero.

Figure 5 shows the ground motion recorded at surface ground zero (station 13) during the collapse. At this amplification, the individual explosive sources in the pillars are not visible, but failure of the pillars and the mine back (roof) is indicated by the early high-frequency arrivals on the top trace. These failure signals ride on top of a long-period signal indicating an initially upward motion interpreted as the formation of a large, horizontally oriented tensile crack (Yang et al., 1998), opposite to implosional source mechanisms commonly observed for large, natural collapses (e.g., Pechmann et al., 1995; Boler et al., 1997). This is followed by strong downward motion associated with the impact of the released material. Ground motion associated with pillar blasting can be seen if we amplify the signal immediately preceding the collapse, as shown by the lower trace in Figure 5. During collapse, peak acceleration reached 300 cm/s^2 at surface ground zero and fell to 20 cm/s^2 at station 5, at a distance of 1.1 km. Peak velocities were 7 cm/s and 0.5 cm/s, respectively.

The collapse was observed at regional seismic stations, the most distant just over 900 km away. Coda lengths of 150 s measured at stations EYMN and TBO, 202 and 213 km distant, respectively (Figure 1), yielded a body-wave magnitude (m_{bLg}) of 3.1 for the collapse event, using a scale developed for New England (Chaplin et al., 1980). We consider this value to be an upper bound because L_g -coda attenuation is slightly higher in New England than in the north-central US (Singh and Herrmann, 1983). Using L_g data from EYMN, a value of 2.8 was obtained (H. Patton, personal communication, 1997), consistent with the upper-bound m_{bLg} from the coda durations.

It is instructive to estimate the mass of falling material that would produce an m_{bLg} 2.8 collapse event. From moment tensor studies, Yang et al. (1998) note a free-fall time, or interval between fracture and impact phases of the collapse, of 0.6 s. This implies the free-fall distance is 1.8 m. Room heights are 3 m; the shorter fall results from the extra volume occupied by pillar rubble and bulking of fractured material from the mine back (roof). Using an m_{bLg} of 2.8 and the free-fall distance of 1.8 m, we estimated the mass of falling material to be $5.7 \times 10^7 \text{ kg}$, following the method of Taylor (1994). Taking the full panel area ($2 \times 10^4 \text{ m}^2$) as an estimate of the collapsed area, a density of 2.6 gm/cm^3 and assuming a uniform thickness of the displaced material gave a thickness of 1 m.

Clearly, confinement of collapse to a smaller area would result in a proportional increase in the thickness. These estimates must be considered approximate.

AFTERSHOCKS

We observed intense aftershock activity following the collapse. The first hour of data from surface ground zero (station 13) is shown in Figure 6. We counted just over 4000 events in 15 hours at this station. Event rate approached 170 per minute at 6 minutes and fell to under 4 per minute in two hours. The rapid decay in event rate points out the difficulty of performing an effective aftershock study if mobilization were to have occurred in response to the collapse. The aftershock rate fit a modified Omori law (Utsu et al., 1995): $\text{rate} = 560 \cdot (\text{time} - 0.01)^{-1.3}$, with time in hours (Figure 7). The fit was applied to data between 6 minutes and 15 hours after the collapse. For times less than 6 minutes, counting was incomplete and for time greater than 15 hours, an instrument malfunction increased noise levels and biased the counting. The decay factor of 1.3 falls within the range obtained for earthquakes. The subtractive, time-offset term of .01 is unusual, but may not be significantly different from zero.

Aftershock Source Characteristics

The aftershock sequence produced a variety of signals. Most events generated high frequencies (up to 100 Hz) and both compressional and dilatational P-wave arrivals. A second class of events generated only dilatational P-waves, often of much lower frequency (10 Hz); a third class, only compressional P-waves. We classified events based on these polarity patterns as shear-slip, implosional and tensile, respectively. Implosional events may include closing crack mechanisms. Combined mechanisms may also be important (Wong and McGarr, 1990); however, some studies have shown mine events tend to be dominated by one style of deformation, be it volume change or shear slip (McGarr, 1992b). To classify an event as implosional or tensile, we required that many stations trigger and collect data (most often eight stations or more, the weakest triggered as few as five) and that all unambiguously determined polarities be the same. To classify an event as shear-slip, fewer stations were required, as long as both compressional and dilatational polarities could be determined. Only the largest and highest signal-to-noise events qualified for classification.

We identified 41 events as shear-slip based on P-wave polarity patterns. Data from a large shear-slip event is shown in Figure 8. This event will be referred to as event A1 in later text and figures. For events classified as shear slip, compressional arrivals were most often observed at stations closest to ground zero and mixed polarities at intermediate

distances. These observations indicate thrust-type, shear-slip motion. The shear-slip events could be further subdivided based on polarity patterns. The largest group generated upward motions at stations 1, 2 and 13, downward at station 7. Event A1 is a member of this group. A second group of events produced the same pattern except for downward motions at station 1 and an occasional upward motion at station 7. We will choose a large event (246:22:58:28.316 UTM) to represent the second group (not shown); this event will be referred to as event A2. Events A1 and A2 will be used later to determine focal mechanisms for the two groups.

A total of 18 events were large enough to be observed at most stations and exhibited all dilatational motions, consistent with an implosional source mechanism. These events also produced significant S-wave arrivals. Eight of these events generated distinctive, low-frequency (10 Hz) waveforms; an example is shown in Figure 9. This event will be referred to as event B in later text and figures. Only two large events were found that generated all compressional arrivals, indicating expanding source mechanisms, most likely tensile failure. Clearly, counting may be less complete for events classified as implosional or tensile because of the more stringent requirements we had to impose.

Differences between events A1 (shear-slip) and B (implosional) are apparent in their surface-ground-zero, P-wave spectra (Figure 10). Spectra were taken from 0.5 s segments of station 13, instrument-corrected, vertical component data, after applying a Hanning taper centered on the P-wave pulse. We corrected for the free surface by dividing by 2. No Q correction was applied because of the short travel distances and relatively competent material. The implosional event generated a corner frequency of 8 Hz and a high-frequency, ω^{-2} decay. The corner frequency for the shear-slip event was more difficult to estimate. We adopted a corner of 60 Hz; however, a corner between 10 and 20 Hz could also be argued. We choose the higher corner because it is more representative of the frequency content of the initial ground motion (Figure 8). Such double-corner events are not uncommon in the White Pine data set and may represent a sum of high- and low-corner, or shear and implosional source types. We also see many high-corner events that follow the more classical, ω^{-2} shape. Finally, the two tensile events generated high-frequency signals (not shown), similar to the shear-slip events.

To further investigate aftershock source types, we assigned corner frequencies (f_0) and low-frequency asymptotes (Ω_0) by inspection for station-13 P-waves from 201 large events, in the manner described above.

The 201-event data set contains all events recorded by a minimum of three stations as specified by the requirements of the location studies. Spectra were analyzed in a blind manner, without knowing event classification, to avoid biasing the results. Assuming a shear-slip source, moment (M_0) and source radii (R) were then calculated using standard techniques (e.g., Hanks and Wyss, 1972):

$$M_0 = 4 \pi \rho c^3 r \Omega_0 / h,$$

$$R = 1.97 c / 2 \pi f_0,$$

where ρ is density (2.6 g/cm³), c is P-wave velocity (3.8 km/s), r is source-receiver distance (300 m), and h is an average radiation coefficient of 0.39 for P waves (Spottiswoode and McGarr, 1975; Boore and Boatwright, 1984). Results show moments ranging from 10^{15} to 10^{17} dyne-cm for shear-slip events (Figure 11), or moment magnitudes of -0.8 to 0.5 (Hanks and Kanamori, 1970). Event A1, the large shear-slip event shown in Figure 8, has an M_w of 0.3, over two orders smaller than the magnitude (m_{bLg}) of the collapse itself. Source radii estimates range from 10 to 50 m for shear-slip events, with most radii falling below 30 m. Source radii calculated using this source model can be overestimated, based on studies comparing with independent measurements in mines (Gibowicz et al., 1990). Stress drops ($\Delta\sigma$) were calculated based on the circular crack model of Brune (1970),

$$\Delta\sigma = 7/16 M_0 / R^3.$$

Lines of constant stress drop are included in Figure 11.

Clearly, source parameters for non-shear events could be re-evaluated using more appropriate models; however, the stress drops as calculated will be useful for classification purposes as they reflect the relationship between moment and source dimension in one parameter. Stress drops are low, 0.1 to 1 bar for the shear-slip events, typical of many mine-related events (Gibowicz et al., 1990), but an order of magnitude larger than the implosional events, revealing a nice separation between event types as classified. Past studies have shown that stress drops can separate shear-slip and isotropic (explosion) events (Cong et al., 1996), although, the sense of separation is opposite to that observed here. In this study, the small stress drops for implosional events partly result from their large source dimensions (roughly 100 m), reflecting possible involvement of the collapsed cavity in the source process.

In Figure 11, a number of unclassified events fall in the low stress-drop range, suggesting larger numbers of implosional events may have occurred than were originally classified. One implosional event falls with the shear-slip events. This event generated a prominent double-corner spectrum, implying a combined shear-implosional mechanism as described

above; the higher corner was chosen during processing. For the smaller shear-slip events, we see a hint of departure from constant-stress-drop scaling at high frequencies. This is an artifact caused by the anti-aliasing filter limiting corner frequencies for small events.

The sequence of aftershocks shows temporal clustering to be common in the White Pine data set (Figure 12). Clusters often contain only one event type. The first cluster at one minute contains five shear-slip events and a number of unclassified events of similar stress drop. At five minutes, an isolated implosional cluster of four events occurs. Later in the sequence, we see more clusters of shear-slip events. However, a cluster of implosional and shear events initiates at six minutes, while an implosional event accompanied by five unclassified events of similar stress drop, as well as a number of shear events, occurs at two hours. The tendency towards temporal grouping of similar stress-drop events, including the unclassified ones, supports extending the source-type classification based on stress drop, as discussed above.

Aftershock Location Procedures

We next prepared to locate the White Pine aftershocks by collecting P- and S-wave arrival times. For all events that were detected by three or more stations, arrival times were determined manually from a display of the vertical, radial and transverse components of motion. Radial and transverse components were obtained by rotating to the direction of ground zero. Five arrival-time quality levels (0-4) were also assigned at this stage: excellent, acceptable, fair, poor and “guess;” only excellent and acceptable arrivals were later used to locate events.

Arrival-time data quality decayed rapidly with distance from ground zero. For the innermost three stations (within 300 m of ground zero), the chance of obtaining a useable arrival time was 70% or so, depending on the specific station and phase. Data rates dropped to 30% at intermediate distance stations (300 m to 600 m) and to 10% or so at the outermost stations (over 1000 m). These percentages were calculated with respect to the number of three-station events, as defined above. On average, such events yielded four P- and four S-wave arrivals, giving a total of eight arrival times available for location.

To calibrate the White Pine site, we developed P- and S-wave velocity models of the subsurface and calculated P- and S-wave station corrections. The station corrections accounted for lateral variations in the layer depths, which are known to be significant, as well as variations in velocities and in the thickness of the glacial till layer at the surface. First,

we set up a 320-m-thick layer-over-a-half-space model, obtaining the layer P-wave velocity from a nearby refraction survey (Geosphere, 1995). The layer contained Nonsuch and Freda layers, the half space contained the Copper Harbor conglomerate. Our intention was to locate aftershocks relative to the known position of the first pillar shot. As pointed out, recordings of the pillar shots were of poor signal-to-noise and we could determine reliable first breaks at only the closest four stations (1, 2, 7 and 13). In addition, a reliable zero time was not available due to the use of a 50 ms electronic delay cap ahead of the first shot, which could not be precisely accounted for. To overcome these problems, we first determined station corrections needed to correctly locate the initial pillar shot, using P-wave arrival times from the four closest stations. We then located two well-recorded aftershocks using P-wave arrivals and corrections at the same stations. Arrivals from the located aftershocks allowed us to determine the remaining P- and S-wave velocities by inspection of traveltimes plots. Following this, station corrections were determined by averaging traveltimes residuals for the two events. The final velocities were 3.80 km/s (P) and 1.60 km/s (S) for the Freda-Nonsuch layer, and 5.46 km/s (P) and 3.07 (S) for the Copper Harbor half-space. The contrast between Freda-Nonsuch and Copper Harbor is dramatic, reflecting an increase in rock competency and strength across the interface. The station corrections ranged from -18 ms to 20 ms for P waves and from -41 ms to 29 ms for S waves (Table 1). The station corrections are consistent with known structure; for example, the early arrivals at station 6 result from a shallowing interface in that direction. This structural information was taken from a three-dimensional model of the mine on display at the White Pine headquarters.

We obtained microearthquake locations using an iterative, damped-least-squares (Geiger's) method, employing the velocity model and station corrections described above. Arrival time data were weighted by $1/T$, where T represents data error estimates of 1.5 ms for P waves and 5 ms for S waves. These values matched RMS arrival-time residuals reasonably well. Because initial results occasionally yielded large residuals, we added a re-weighting scheme (Scales et al., 1988), which approximates the minimum L_1 norm solution. The location calculation also included an estimate of the standard location-error ellipsoid, using T , above, as estimates of the data error.

For selected groups of events that generate similar waveforms, we can obtain more precise relative locations. This is done by choosing arrival times at the same point in the waveform for all similar events, then adjusting station corrections to hold the position of a well-recorded, master

event fixed to its original location. Based on residuals, we estimate that data errors improve to 1 and 2 ms for P and S waves, respectively, resulting in precise locations relative to the master event. Relative location studies have proven useful for understanding joint structures along which geothermally induced microearthquakes occurred (Phillips et al., 1997) and have been used successfully to identify failure surfaces in mining-induced seismic data (Spottiswoode and Milev, 1998).

Aftershock Location Results

Map and cross-section views of 135 aftershock locations are shown in Figure 13. These aftershocks were required to have six or more arrival times and magnitude of the major error-ellipsoid axis less than 20 m.

The map view shows a distribution of aftershocks concentrated along the western edge of the collapsed panel open to the mine. Activity is absent within 50 m of most un-mined faces. The cross-section views show an active zone just under 100 m thick, bottoming at mine level. A few events locate 20 m or so below mine level and may be mislocated. In the east-west cross section, events define a triangular prism with upper edges dipping 45° to the east and nearly vertical to the west. Over 90% of the locatable events occurred within two hours of the collapse. The latter 10% occurred during isolated swarms of activity through the remaining 36 hours of network operation. The major axes of the standard (one- σ) location-error ellipsoids pointed in northerly, near-horizontal directions, with a scatter of $\pm 35^\circ$ and an average length of 10 m. The predominance of north-trending major axes results from an east-west distribution of the closer in stations (Figure 3). Error-ellipsoid aspect ratios averaged 1.6 (major/intermediate) and 2.6 (major/minor).

Event type and stress drop strongly correlate with location depth (Figure 14). Implosional events are found over a narrow depth range just above mine level, while shear-slip events occur throughout the active depth range and dominate at shallow depths. Unclassified events follow the same, overall pattern. In particular, only high stress-drop events, corresponding to shear slip, are found at shallow depths. This augments the population of shear-slip events at shallow depths, which will be important to later arguments concerning stress redistribution after collapse.

We relocated the 41 shear-slip events using the master-event techniques as described above. Results are shown for the two polarity-pattern event families in Figure 15. For the A1 event family, relocations show a planar patch of activity of length 50 m, striking $N16^\circ W$ and dipping

75° to the east. These events all follow event A1 and form an aftershock sub-sequence. Event A1 locates near the southern end of the linear trend in map view. The southern end was active initially, then activity migrated steadily northward. The estimated source dimension of event A1 (diameter 40 m) is similar to the length of the linear zone. Based on relative data errors of 1 ms for P waves and 2 ms for S waves, standard error ellipsoids are reasonably isotropic with median length of the major axes measuring 5 m. Because the vertical dimension of the active plane is only 20 m, the interpreted dip angle must be considered somewhat uncertain. Location results for the second family of events (A2) aligned directly above the western boundary of the collapsed panel.

We also relocated the 18 implosional events in the same manner (Figure 16). Relocations emphasize the tight depth range at the bottom of the seismic zone over which these events occurred. The relative depths are more important than their absolute depths, which are governed by the initial location of the master event. Spatial clustering of the implosional events is evident in the map view. Furthermore, events of similar corner frequency cluster together, perhaps indicating repetitive failures of the same source. As noted earlier, implosional events also cluster temporally; for example, four of the low-frequency events directly under station 13 occurred within 11 s of each other. Also included in Figure 16 are original locations of the two tensile events. These events are shallower than the implosional events and locate towards the outside edge of the aftershock zone. These events have mechanisms similar to that of the main collapse (Yang et al., 1998) and may represent continued collapse via tensile failure around the edges.

Aftershock Source Mechanisms

We obtained focal mechanisms for two shear-slip type events, each representative of a group of events displaying similar polarity patterns. The first event was the large aftershock (event A1, Figure 8), representative of the most populous polarity-pattern group that generated upward motions at stations 1, 2, and 13 and downward motions at station 7. A second event (event A2) was representative of the second largest polarity-pattern group that generated upward motions at stations 2 and 13, downward motions at station 1 and variable motion at station 7. Focal mechanisms were obtained using P- and S-wave polarities and amplitude-ratio data, employing a code available over the web (Snoke et al., 1984). We did not trust turning ray take-off angles calculated for the more distant stations and restricted the analysis to seven close-in stations (1, 2, 6, 7, 9, 10 and 13). This was done because the velocity model was calibrated for location purposes and structure that may be important for

calculation of take-off angles, especially for turning ray paths, was ignored or taken up in the bulk station corrections. In addition, because of the high velocity contrast, small changes in location depth could cause takeoff angles to flip between upgoing and turning rays for stations near the cross-over distance (roughly 700 m for these two events).

After rotating to radial and transverse components based on the event location, we measured P-, S_v - and S_h -wave polarities, and peak-amplitude P/S_h , P/S_v and S_h/S_v ratios directly from the traces. The P and S waveforms were nicely partitioned between vertical and horizontal components, respectively, due to steep angles of incidence at the surface (Figures 8 and 9). We assumed free-surface and instrument corrections would cancel in the amplitude ratios and did not perform them. These measurements may be considered rough; however, we allowed a factor of four misfit in the ratio data when fitting focal mechanisms. The code performed a grid search and returned all mechanisms that fit the data, allowing a fixed number of polarity and ratio mismatches. For both events, we obtained well-constrained solutions by requiring all P- and S-wave polarities be satisfied, while allowing one amplitude-ratio mismatch. We plot the results in upper, rather than lower hemisphere stereo projection so the station patterns will be similar to their geographical distribution.

Double-couple focal mechanisms for events A1 and A2 indicate thrusting along north-south striking planes (Figure 17). Differences between events occur mainly in their dip angles. P-wave polarities alone were insufficient to constrain focal mechanisms for these events. The event A1 result illustrates the extra constraints provided by the S-wave polarities (Figure 17a). The near-vertical T axis is constrained by S-wave motions at the four surrounding stations. Weak S_v and S_h at station 7 and strong S_h at stations 9 and 10 constrain the P axis to nearly east-west. Similar observations can be made for event A2.

For event A1, we choose the near-vertical plane as the true slip plane because it is oriented nearly parallel to the plane defined by its own aftershock subsequence (Figure 15); although, as noted, the dip of this feature may not be well determined. In addition, generalized structure maps of the mine show a number of high-angle faults, the closest striking slightly east of north, with an offset of 43 m down to the east side, 1 km to the west of the collapsed panel (Mauk et al., 1992). Even though the sense of slip is in the opposite direction, the presence of north-striking, near-vertical planes of weakness further supports the choice of the near-vertical plane as the true slip plane of event A1 (Figure 17a). Both planes of event A2 (Figure 17b) are consistent with the known, regional, east-

west compressive stress; however, we note the top edge of the seismic cloud dips 45° to the east (Figure 13), similar to the east-dipping slip plane. Location patterns obtained using just close-in stations 1, 2 and 13, while containing fewer events, emphasize this east-dipping structure even more (not shown). We see no evidence supporting either slip plane in relocation patterns of events similar to event A2 (Figure 15). To date, we lack information about joint structures in the Nonsuch layer above the collapsed panel. This would clearly help to evaluate our conjectures.

We also analyzed the large implosional event (event B, Figure 9) using a time-dependent moment tensor inversion (Stump and Johnson, 1977), the same technique applied to study the source mechanism of the collapse (Yang et al., 1998). Results gave diagonally dominant moment-tensor traces (Figure 18), with downward initial motions on all three diagonal components. We decline to interpret the relative sizes of the moment tensor terms because these were found to vary with respect to filtering and the station set included in the calculation. We see delayed fluctuations in the northeast, off-diagonal component (M_{12}), indicating a complex source with non-isotropic components. Decomposition of the moment tensor indicated a range of thrust and strike-slip mechanisms associated with the off-diagonal pulse and we consider the non-isotropic component of the source mechanism unresolved.

DISCUSSION

Source Mechanisms

Seismologists have noted implosional events associated with mining, but were initially unsure how to interpret them (Wong and McGarr, 1990). Wong and McGarr (1990) did speculate that a shear-implosional mechanism was the most plausible, and evidence supporting implosional sources has continued to accrue (Gibowicz et al., 1990; McGarr, 1992a,b; Stickney and Sprenke, 1993; Baker and Young, 1997). At White Pine, relative locations show that implosional events occurred over a very narrow depth range, 20-30 m above the mine level (Figure 16). Given our estimate of the thickness of displaced material of 1 m and the possibility of systematic mislocation from our calibration procedure, it is reasonable to conclude that implosional events occurred along the boundary between intact rock and rubble. This would be consistent with the required reduction in void space.

An implosional source could result from the collapse of an open space along a jagged interface, or the failure of an unfragmented pillar or a highly stressed piece of rubble. Pillar failure could cause mine back (roof) and floor to converge, the large source dimension resulting in the low

corner frequencies and stress drops we measured for implosional events (Figures 10, 11).

A cluster of low-frequency implosional events falls close to an edge pillar that was identified as remaining partially intact during post-collapse inspection (Figure 16). Incomplete demolition could be caused by an earlier charge dislodging another firing mechanism prior to activation (Forsyth, 1995). We expect extreme stress concentration in and around such a pillar. If implosional sources are associated with incomplete pillar removal, similar events in the interior of the panel might indicate other partially intact pillars that could not be viewed after collapse (Figure 16).

The implosional events found at White Pine produced dilatational signals similar to those of large mine collapses (e.g., Pechmann et al., 1995; Boler et al., 1997). A suggested implosional aftershock mechanism, partial pillar failure coupled with convergence of mine back (roof) and floor, is what might be expected for the initial stage of wholesale, natural mine collapse. In contrast, the main collapse at White Pine was found to be very different from natural collapse. Specifically, moment-tensor inversion of the close-in records at White Pine, indicated an expanding source mechanism, which was interpreted as an opening tensile crack (Yang et al., 1998). Yang et al., (1998) believe the sudden, man-made origin of the collapse caused previously undeformed material to part on time scales that could be measured in the seismic band. The competent character of the rock also favors the formation of a tensile crack by preventing extension of the collapse to the surface. However, the aftershocks occurred in response to stress redistribution on periods of minutes to hours and, in this sense, may be considered similar to natural collapse. These time periods allow deformation to occur outside the seismic band. Low-amplitude signals precede many White Pine events, perhaps related to aseismic deformation. The low stress drops measured for shear-slip events (1 bar or less) are also consistent with the occurrence of aseismic deformation. Thus, response to time scales of stress redistribution, as suggested by Yang et al. (1998), may form the basis for a unifying description of the White Pine sequence that includes the unusual mechanism of the main collapse.

From our location, source mechanism and source parameter studies, we conclude the White Pine sequence is composed of implosional events occurring at mine depths and north-striking, high- to intermediate-angle thrusting events and less commonly, tensile events, occurring at mine depths and above, near the western edge of the collapsed panel. Our results are similar to those obtained at the Underground Research Laboratory, Canada, where implosional-shear events were associated with

the collapse of excavation holes along the tunnel edge, tensile-shear events occurred ahead of the tunnel face and dominantly shear events slipped along existing planes of weakness in areas of high deviatoric stress (Baker and Young, 1997). Similarities are especially noteworthy given the nearly two orders of magnitude difference in scale between experiments.

Stress Redistribution

At White Pine, thrust faulting along north-striking planes is consistent with the strong, east-west oriented horizontal stress known for the region (McGarr and Gay, 1978; Zoback and Zoback, 1980). We believe failure was facilitated by a reduction in confining, vertical stress following collapse, increasing deviatoric stress and resulting in slip, presumably along pre-existing joint surfaces. Before we accept this model of aftershock generation, we must understand why events are not induced below the collapsed panel, where stresses should be high, given the nearly symmetrical geometry, and why events concentrate along the western edge of the panel as opposed to being distributed more equally throughout.

We believe the asymmetrical aftershock distribution above and below the panel is primarily controlled by the strengths of the rock layers. The panel lies along the interface between Nonesuch Shale and Copper Harbor Conglomerate. From our velocity calibration work, we found P- and S-wave velocities increased 43% and 92% across this boundary, respectively. These are high contrasts for geological boundaries, indicating an increase in competency of material that should be reflected in its response to high deviatoric stress. In addition, we expect slightly higher vertical, confining stress below the mine through loads imposed through the rubble zone, another factor in reducing the potential for activity at depth.

The asymmetrical, lateral distribution of events could be related to the siting of the collapsed panel at the edge of the mine, surrounded by intact rock on three faces. It is theoretically understood and commonly observed that pillars close to mine faces support less load than those further away. At White Pine, convergence between mine back (roof) and floor is rarely observed within 100 m of the face during drift extension. This is qualitatively consistent with models of overburden load supported by a beam of material above the pillars, as opposed to each pillar supporting all the overburden between it and its neighbors. If pre-collapse pillar stress increased away from the mine faces in the collapsed panel at White Pine, stress changes should be more dramatic, producing higher potential for slip, along the western edge. Another possible effect is the firing pattern, which started in the middle of the western edge and

proceeded toward the mine face. Fracturing and collapse of the mine back (roof) should have initiated along the western edge, producing slip along nearby surfaces that could then slip more easily later on. Incomplete destruction of the pillars at the end of the firing pattern could also be a factor, but is not required to account for the asymmetrical aftershock pattern.

In-situ measurements of stress changes in pillars adjacent to the collapsed panel were compared to predictions of pseudo-3D models by Forsyth (1995). The modeled stress changes depend on the extent of a “de-stressed” region, or arch, directly above the collapse, defined as any material whose load was supported through the rubblized zone rather than through the adjacent pillars or un-mined faces. The geometry, primarily the height, of this zone must be specified prior to modeling. Height estimates are based on experience but are known to be a source of uncertainty in the modeling. At White Pine, the vertical dimension of the de-stressed zone was set at 110 m after specifying an equilateral triangular cross-section along the short span (east-west) of the panel (Figures 13, 19a; Forsyth, 1995). Surface leveling studies showed no deformation associated with collapse, consistent with a de-stressed zone confined to the subsurface. The model predicted post-collapse stresses on adjacent pillars that matched well with measurements, except for the pillars immediately adjacent to the collapsed panel (first row) where measured stress changes were lower than model predictions (Forsyth, 1995). Because of the importance of avoiding a cascading pillar failure that could do significant damage to the mine, it may be best that the modeling overestimated the effect of the collapse on the adjacent pillars. However, the distribution and source mechanisms of the aftershocks may help understand why overestimates were made.

Any thrusting aftershocks, if caused by a decrease in vertical stress following the collapse, should fall within the de-stressed zone used in modeling the stress redistribution. West of the de-stressed zone, vertical stress would have increased slightly, in response to the additional load from material above the collapsed panel, thus reducing deviatoric stress. The vertical thickness of the aftershock zone was nearly the same as that of the assumed de-stressed zone (Figure 13). However, activity was much heavier above the open, western panel edge. If the de-stressed zone were modified to include the aftershock distribution (Figure 19b), more load would shift to the un-mined faces, reducing modeled stresses along the western edge of the collapsed panel, possibly enabling stress measurements in the first row of pillars to be matched more closely. Clearly, a quantitative comparison between modeled stresses and the

distribution of aftershocks and slip directions will help to modify and develop these ideas further.

CONCLUSIONS

The explosively induced collapse of a panel in an underground room-and-pillar mine generated seismic signals observed at distances over 900 km. The collapse magnitude was estimated to be m_{bL_g} 3.1, at most, from coda lengths and m_{bL_g} 2.8 from L_g amplitudes at regional stations. The L_g value led to rough estimates of the mass and thickness of the displaced material of 5.7×10^7 kg, and 1 m, respectively.

Seismic records from a 2-km aperture, close-in array showed that the individual explosive charges emplaced in the pillars produced weak seismic signals, presumably due to the effects of decoupling and delay firing; however, the failure of the pillars and the material above the working level as well as the impact of failed material produced strong signals. Previous work found these signals consistent with an expanding source mechanism, interpreted as a tensile failure along a horizontal crack (Yang et al., 1998). This differs from large, natural collapse sources, which are dominantly implosional.

Intense aftershock activity followed the collapse; we counted over 4000 events at surface ground zero in the first 15 hours. The rate of occurrence could be described by the modified Omori law with an exponent of 1.3. We identified 41 shear slip, 18 implosional and 2 tensile events in the aftershock sequence, based on P-wave polarity patterns. Standard source parameters indicated stress drops of 0.1 to 1 bar for shear slip and tensile events and 0.01 to 0.1 bar for implosional events. The lower stress drops for implosional events were produced by relatively low corner frequencies, perhaps related to larger source dimensions that include the collapsed cavity. The separation between source types suggested the stress drops could be used to classify events of unknown source type. This was supported by the temporal clustering of similar stress-drop events with their known counterparts. Shear-slip aftershock moments ranged from 10^{15} to 10^{17} dyne-cm, moment magnitudes, -0.8 to 0.5 and source radii, 10 to 50 m with most less than 30 m.

Aftershock locations defined a zone of activity less than 100 m thick, bottoming at mine level, offering no evidence of deformation extending to the surface. A large contrast in rock competency, thus material strength, likely confined activity to the layer above the panel. Activity was heaviest above the western, open edge of the collapsed panel. This could result from higher initial pillar stresses, thus more dramatic change, away from mine

faces, or from effects of the firing pattern, which initiated under the area of high activity. Shear-slip events were found throughout the active depth range, while implosional events were confined to a narrow range, just above the mine level, possibly associated with the collapse of void space along a jagged interface between intact rock and rubble, or the failure of incompletely demolished pillars or highly stressed rubble. For events of unclassified source type, only higher stress drops, implying shear slip, were found in the shallow half of the active zone. Focal mechanisms of two large shear-slip events indicated north-striking, intermediate- to high-angle thrusting.

Aftershock locations defined a zone of stress redistribution and deformation following the collapse. The presence of thrust events above the western edge of the collapsed panel suggested an asymmetrical de-stressed zone, or arch, consistent with the low stresses measured in the first row of pillars relative to stresses predicted by post-collapse models.

ACKNOWLEDGMENTS

The support received from White Pine Mine personnel was crucial to the success of our field deployment. Special thanks go to Daniel St. Don, Steve Brooks and Jochen Tilk. We also thank CL Edwards, Diane Baker, Roy Boyd, Keith Kihara and Keith Dalrymple for help with data acquisition and Hans Hartse for retrieving seismic data from regional stations. We are grateful to Steve Taylor and Howard Patton for discussions about unusual source mechanisms. The focal mechanism code was provided by J.A. Snoke: <http://www.geol.vt.edu/outreach/vtso/focmec/>. Ivan Wong and Chris Young provided careful reviews of the manuscript. Data processing and mapping was carried out using SAC and GMT software. This work is in support of the DOE Comprehensive Test Ban Treaty Research and Development Program, ST482A, and was performed at Los Alamos National Laboratory under the auspices of the U.S. Department of Energy, Contract Number W-7405-ENG-36.

REFERENCES

- Baker, C. and R.P. Young (1997). Evidence for extensile crack initiation in point-source time-dependent moment tensor solutions, *Bull. Seism. Soc. Am.* **87**, 1442-1453.
- Boler, F.M., S. Billington, and R.K. Zipf (1997). Seismological and energy-balance constraints on the mechanism of a catastrophic bump in the Book Cliffs coal-mining district, Utah, USA, *Int. J. Rock Mech. and Min. Sci.* **34**, 27-43.
- Boore, D. and J. Boatwright (1984). Average body-wave radiation coefficients, *Bull. Seism. Soc. Am.* **74**, 1615-1622.

- Brune, J. (1970). Tectonic stress and the spectra of seismic shear waves from earthquakes, *J. Geophys. Res.* **75**, 4997-5009.
- Chaplin, M.P., S.R. Taylor and M.N Toksoz (1980). A coda-length magnitude scale for New England, *Earthquake Notes* **51**, 15-22.
- Cong, L.L, J.K. Xie, and B.J. Mitchell (1996). Excitation and propagation of L_g from earthquakes in central Asia with implication for explosion/earthquake discrimination, *J. Geophys. Res.*, **101**, 27779-27789.
- Forsyth, W. (1995). Modeling results for Unit 43 test panel. Report to Copper Range Company, Golder Associates Ltd.
- Geosphere, Inc. (1995). Seismic reflection survey for northeast mine expansion planning, White Pine Mine. Report to Copper Range Company.
- Gibowicz, S.J., H.-P. Harjes, and M. Schafer (1990). Source parameters of seismic events at Heinrich Robert mine, Ruhr Basin, Federal Republic of Germany: Evidence for nondouble-couple events, *Bull Seism. Soc. Am.* **80**, 88-109.
- Hanks, T.C. and H. Kanamori (1970). Moment magnitude scale. *J. Geophys. Res.* **84**, 2348-2350.
- Hanks, T.C. and M. Wyss (1972). The use of body-wave spectra in the determination of seismic-source parameters, *Bull. Seism. Soc. Am.* **62**, 561-589.
- Hasegawa, H.S., R.J. Wetmiller, and D.J. Gendziwill (1989). Induced seismicity in mines in Canada--an overview, *Pageoph* **129**, 423-453.
- Mauk, J.L., W.C. Kelly, B.A. van der Pluijm, and R.W. Seabor (1992). Relations between deformation and sediment-hosted copper mineralization: Evidence from the White Pine part of the Midcontinent rift system, *Geology* **20**, 427-430.
- McGarr, A. (1992a). An implosive component in the seismic moment tensor of a mining-induced tremor, *Geophys. Res. Lett.* **19**, 1578-1582.
- McGarr, A. (1992b). Moment tensors of 10 Witwatersrand mine tremors, *Pure Appl. Geophys.* **139**, 781-800.
- McGarr, A. and N.C. Gay (1978). State of stress in the earth's crust, *Ann. Rev. Earth Planet. Sci.* **6**, 405-436.
- Pechmann, J.C., W.R. Walter, S.J. Nava, and W.J. Arabasz (1995). The February 3, 1995 M_L 5.1 seismic event in the Trona Mining District of southwestern Wyoming, *Seism. Res. Lett.* **66**, 25-34.
- Phillips, W.S., L.S. House, and M.C. Fehler (1997). Detailed joint structure in a geothermal reservoir from studies of induced microearthquake clusters, *J. Geophys. Res.* **102**, 11745-11763.
- Scales, J.A., A. Gersztenkorn, and S. Treitel (1988). Fast L_p solution of large, sparse, linear systems: application to seismic traveltome tomography, *J. Comp. Phys.* **75**, 314-333.

- Singh, S. and R.B. Herrmann (1983). Regionalization of crustal coda Q in the continental United States, *J. Geophys. Res.* **88**, 527-538.
- Snoke, J.A., J.W. Munsey, A.G. Teague, and G.A. Bollinger (1984). A program for focal mechanism determination by combined use of polarity and SV-P amplitude ratio data, *Earthquake Notes* **55**, 15.
- Spottiswoode, S.M. and A. McGarr (1975). Source parameters of tremors in a deep-level gold mine, *Bull. Seism. Soc. Am.* **65**, 93-112.
- Spottiswoode, S.M. and A.M. Milev (1998). The use of waveform similarity to define planes of mining-induced seismic events, *Tectonophysics* **289**, 51-60.
- Stickney, M.C. and K.F. Sprenke (1990). Seismic events with implosional focal mechanisms in the Cour d'Alene mining district, northern Idaho, *J. Geophys. Res.* **98**, 6523-6528.
- Stump, B.W. and L.R. Johnson (1977). The determination of source properties by the linear inversion of seismograms, *Bull. Seism. Soc. Am.* **67**, 1480-1502.
- Taylor, S.R. (1994). False alarms and mine seismicity, an example from the Gentry Mountain mining region, Utah, *Bull. Seism. Soc. Am.* **84**, 350-358.
- United Nations General Assembly, Comprehensive Test Ban Treaty, **A/50/1027**, 26 August 1996.
- Urbancic, T.I., C.I. Trifu, and R.P. Young (1993). Microseismicity derived fault-planes and their relationship to focal mechanism, stress inversion and geologic data, *Geophys. Res. Lett.* **20**, 2475-2478.
- Utsu, T., Y. Ogata, and R.S. Matsuura (1995). The centenary of the Omori formula for a decay law of aftershock activity, *J. Phys. Earth* **43**, 1-33.
- Wong, I.G. and A. McGarr (1990). Implosional failure in mining-induced seismicity: a critical review, in *Proc. Second Int. Symp. on Rockbursts and Seismicity in Mines*, C. Fairhurst (Editor), A.A. Balkema Publishers, Rotterdam, 45-51.
- Yang, X., B.W. Stump, and W.S. Phillips (1998). Source mechanism of an explosively induced mine collapse, *Bull. Seism. Soc. Am.* **88**, 843-854.
- Young, R.P. and S.C. Maxwell (1992). Seismic characterization of a highly stressed rock mass using tomographic imaging and induced seismicity, *J. Geophys. Res.* **97**, 12,361-12,373.
- Zoback, M.L. and M. Zoback (1980). State of stress in the conterminous United States, *J. Geophys. Res.* **85**, 6113-6156.

Table 1. Station locations (Michigan state coordinates) and arrival-time corrections for the 1995 White Pine experiment:

Station	Northing	Easting	P-wave Correction	S-wave Correction
	k m	k m	m s	m s
1	581.346	95.202	10	4
2	581.125	95.010	15	27
3	580.368	94.746	-4	-2
4	580.346	95.166	4	1
5	582.138	95.693	4	-23
6	581.010	95.466	-18	-41
7	581.186	94.512	2	-9
8	581.688	94.275	7	-7
9	581.631	94.427	9	-13
10	581.612	94.516	11	-15
11	581.835	94.455	10	-17
13	581.311	94.959	20	29

FIGURE CAPTIONS

Figure 1: Location of the White Pine Mine, Upper Peninsula, Michigan. Regional stations used in the m_{bLg} analysis are also shown (triangles).

Figure 2: Plan view of underground workings at White Pine. Failed areas of the room and pillar mine are indicated by black patches, including the 1995 induced collapse.

Figure 3: Map of three-component seismic stations (triangles) used to monitor the induced collapse at White Pine. Mined areas are indicated by light gray fill, the collapsed panel by dark gray fill. Axes give easting and northing in Michigan state coordinates.

Figure 4: Map view of delay-fire pattern used to rubblize pillars. Intact rock and pillars are shown in gray. Only pillars that had been planned to be demolished are shown. Annotated contours indicate delay times (ms).

Figure 5: Vertical component of ground motion velocity at surface ground zero (station 13) during collapse. The lower trace has been amplified a factor of 100 to show effects of the pillar blasts. Time is measured relative to the initiation time of the firing sequence.

Figure 6: Station 13, vertical-component seismograms covering the first hour following the collapse. The amplitude scale is fixed, causing larger events to be off scale.

Figure 7: Aftershock occurrence rate (circles) and the modified Omori law fit (line). The RMS amplitude of each aftershock is also plotted (small symbols) on an arbitrary scale to show the time range over which aftershock counting is complete.

Figure 8: Vertical, radial and tangential (left to right) components of ground velocity for a large shear-slip aftershock (M_w 0.3), plotted versus epicentral distance. Each trace is scaled to its maximum amplitude. Time is relative to the origin time determined from the event location (246:22:00:13.414). Dashed lines represent predicted P- and S-wave arrival times. Stations are indicated next to each trace. This event is referred to as event A1 in text and later figures.

Figure 9: Seismograms generated by a large implosional aftershock, origin time 246:23:45:59.983, as in Figure 8. This event is referred to as event B in text and later figures.

Figure 10: Displacement spectra from station 13, vertical component P waves for shear-slip event A1 (top) and implosional event B (bottom). Lighter lines indicate noise spectra obtained with the same window length and shape, as described in the text. Dashed lines indicate ω^{-2} slope.

Figure 11: Moment and M_w versus source radius and corner frequency from P-wave spectra of aftershocks. Symbols represent event types as shown in the legend. Shear-slip events A1 and A2 and implosional event B are labeled. Lines of constant stress drop are included.

Figure 12: Inferred stress drop versus time of occurrence in the aftershock sequence. Symbols represent event types as shown in the legend. Shear-slip events A1 and A2 and implosional event B are labeled.

Figure 13: Map and cross-section views of aftershock locations. Events A1, A2 and B are plotted using larger circles as annotated. The mine and collapsed panel are indicated in the map view. The collapsed panel is shown to scale in the cross-section views. Close-in stations 2 and 13 are indicated by triangles in map view. The dotted triangle in the cross-section view looking north represents the assumed de-stressed zone used in modeling post-collapse stress redistribution.

Figure 14: Event depth versus inferred stress drop of the aftershocks. Symbols represent event types as shown in the legend. Shear-slip events A1 and A2 and implosional event B are labeled. The dashed line represents mine level.

Figure 15: Map and cross-section views of high-precision locations of shear-slip events with polarity patterns similar to event A1 (open circles) and event A2 (x's). Events A1, A2 and the master event (M) are indicated. A close-up, cross-section view looking N16°W is shown at lower right.

Figure 16: Map and cross-section views of high-precision locations of implosional events (circles) and tensile events (x's). Low-frequency implosional events are shown by filled circles, high-frequency events by open circles in the map view. Event B and the master event (M) are also indicated. A pillar that remained partially intact stands along the edge of the collapsed panel as shown.

Figure 17: Upper hemisphere focal mechanisms for two shear-slip events: a) event A1, representative of the most commonly observed polarity pattern group, and b) event A2, representative of the second most commonly observed polarity pattern group. Filled circles represent compressional P waves, open circles, dilatational P waves. Arrows indicate S-wave polarizations. P and T axes are also shown.

Figure 18: Time-dependent moment rate for the implosional aftershock shown in Figure 9. Traces are plotted to the same scale in tensor format. The time axis is included at lower right. Time origin is the event origin time. Annotations indicate maximum trace values (Nm/s).

Figure 19: Cartoons representing cross-section views of stress trajectories and de-stressed zones postulated for the collapse: a) symmetrical de-stressed zone used to model stress redistribution as described in the text, and b) asymmetrical de-stressed zone modified to include aftershocks. By definition, the de-stressed zones encompass material supported through the rubble zone in the collapsed panel. Stress trajectories indicate principal stress directions, analogous to streamlines. These stress trajectories are plotted as if undisturbed maximum principle

stress is vertical; however, a de-stressed zone will also exist in a maximum horizontal principle stress regime.

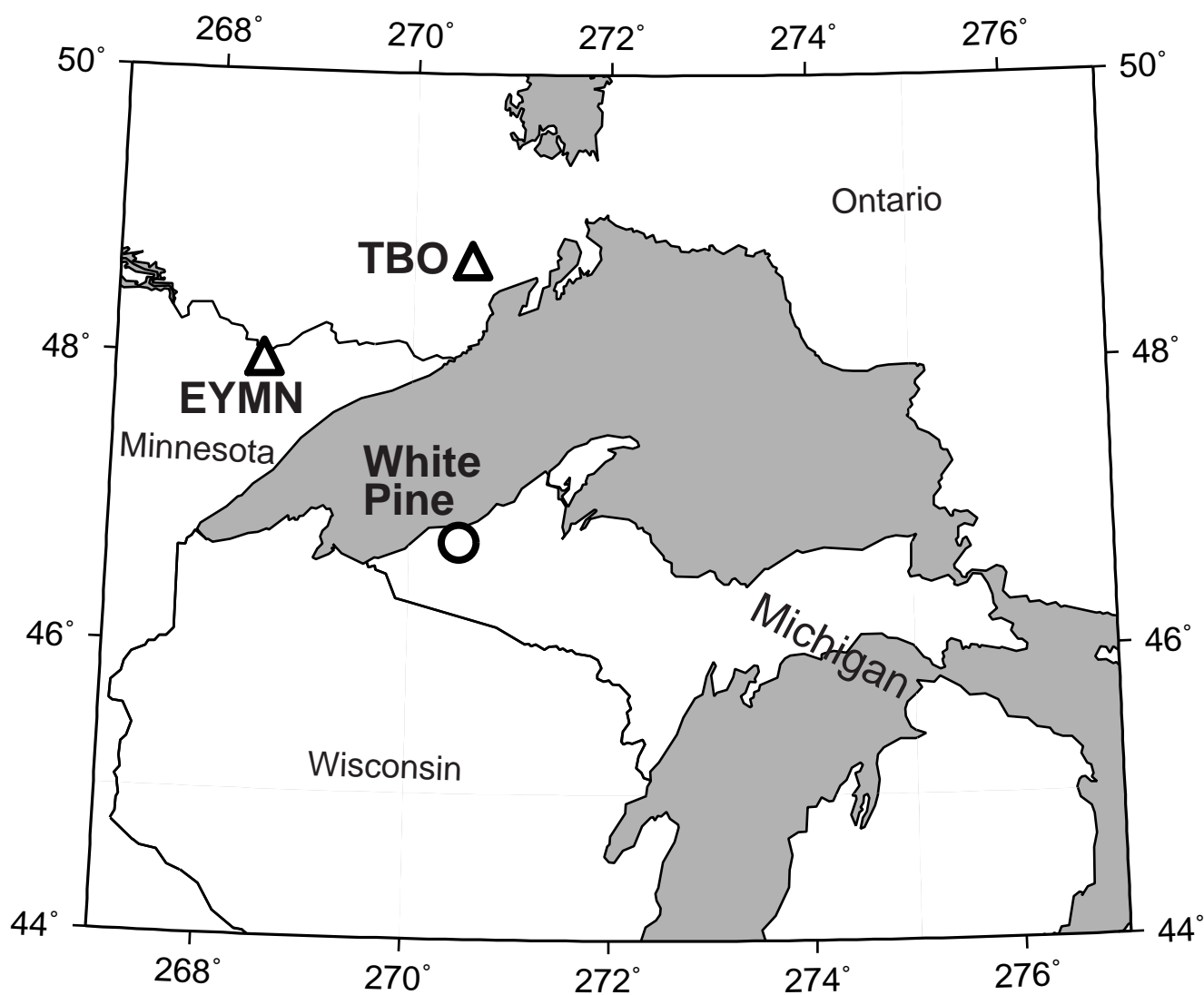


Figure 1

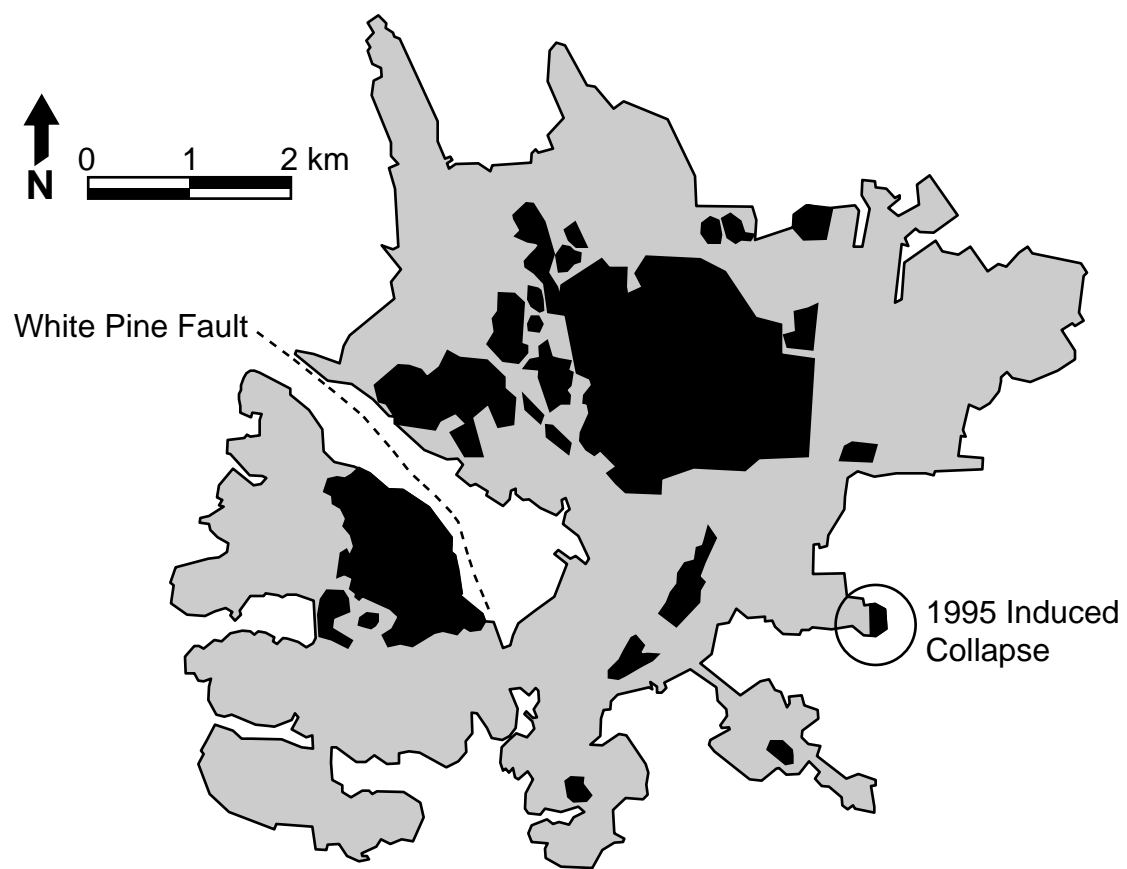


Figure 2

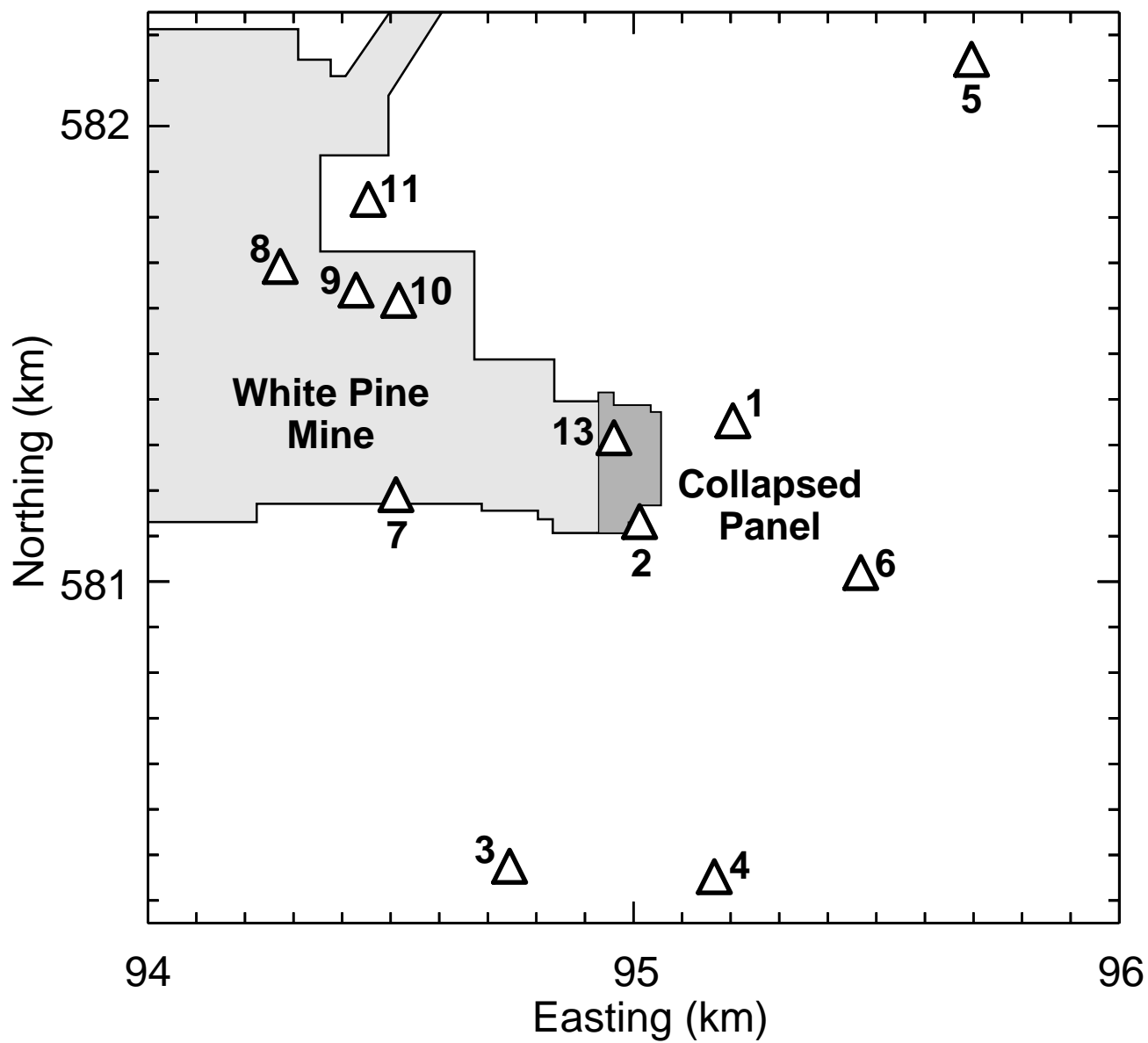


Figure 3

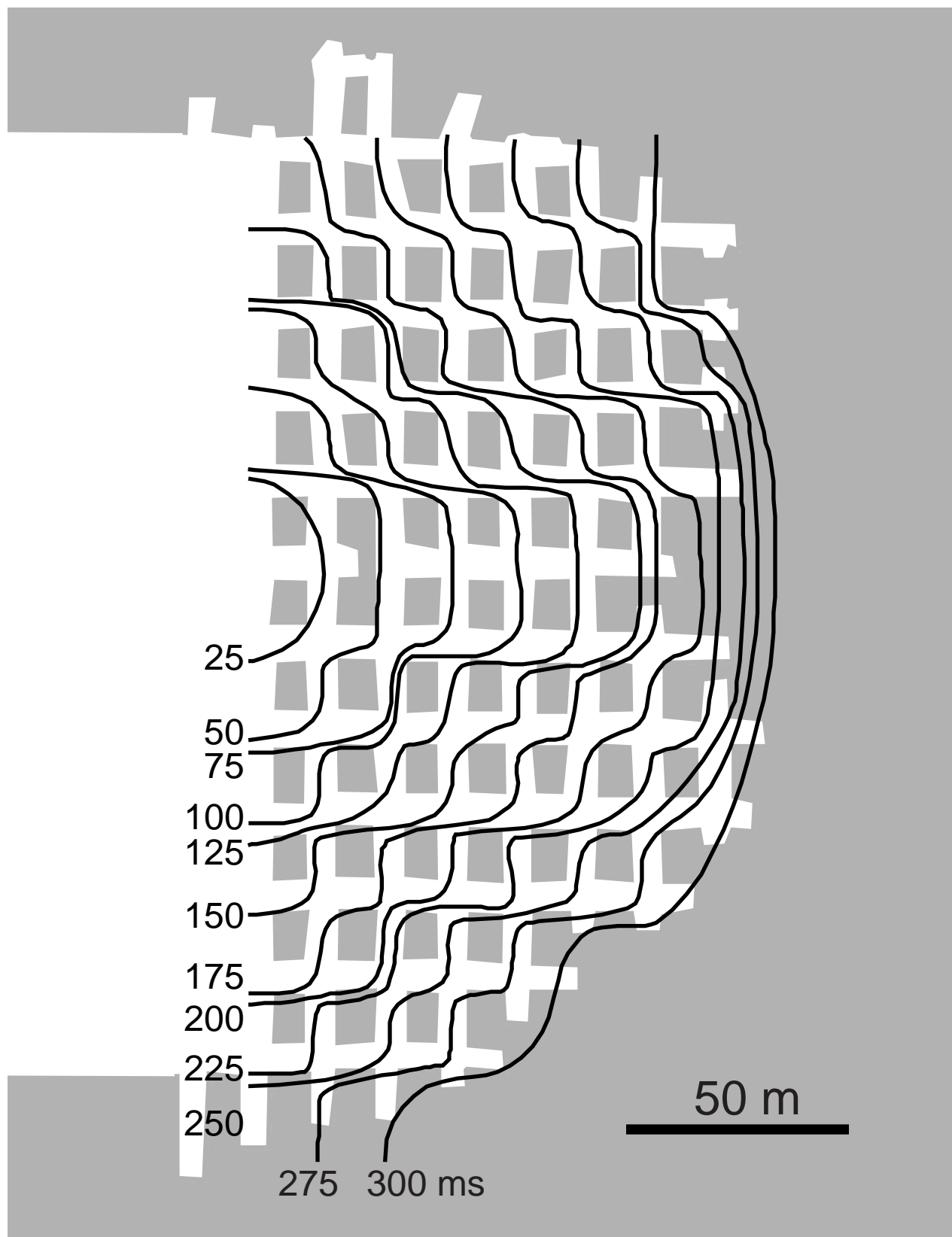


Figure 4

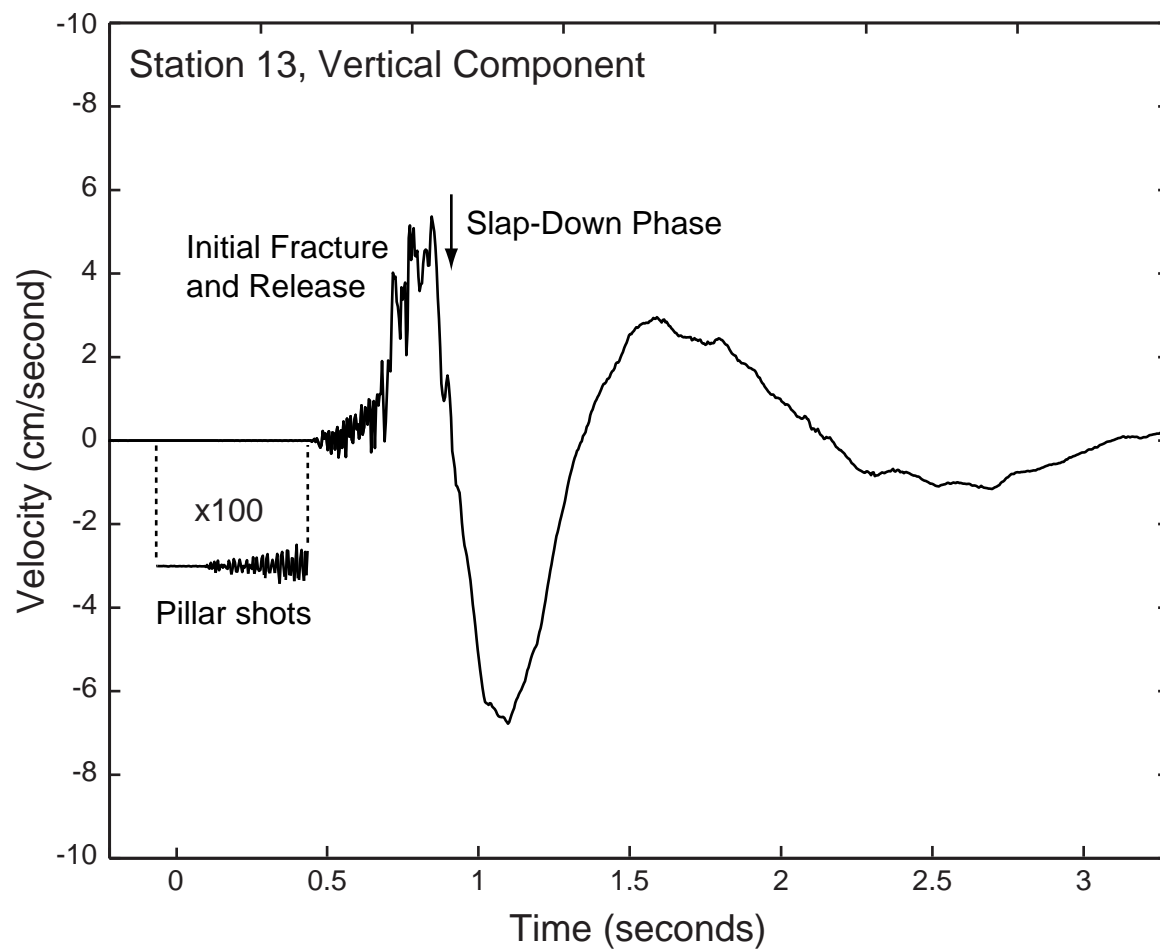


Figure 5

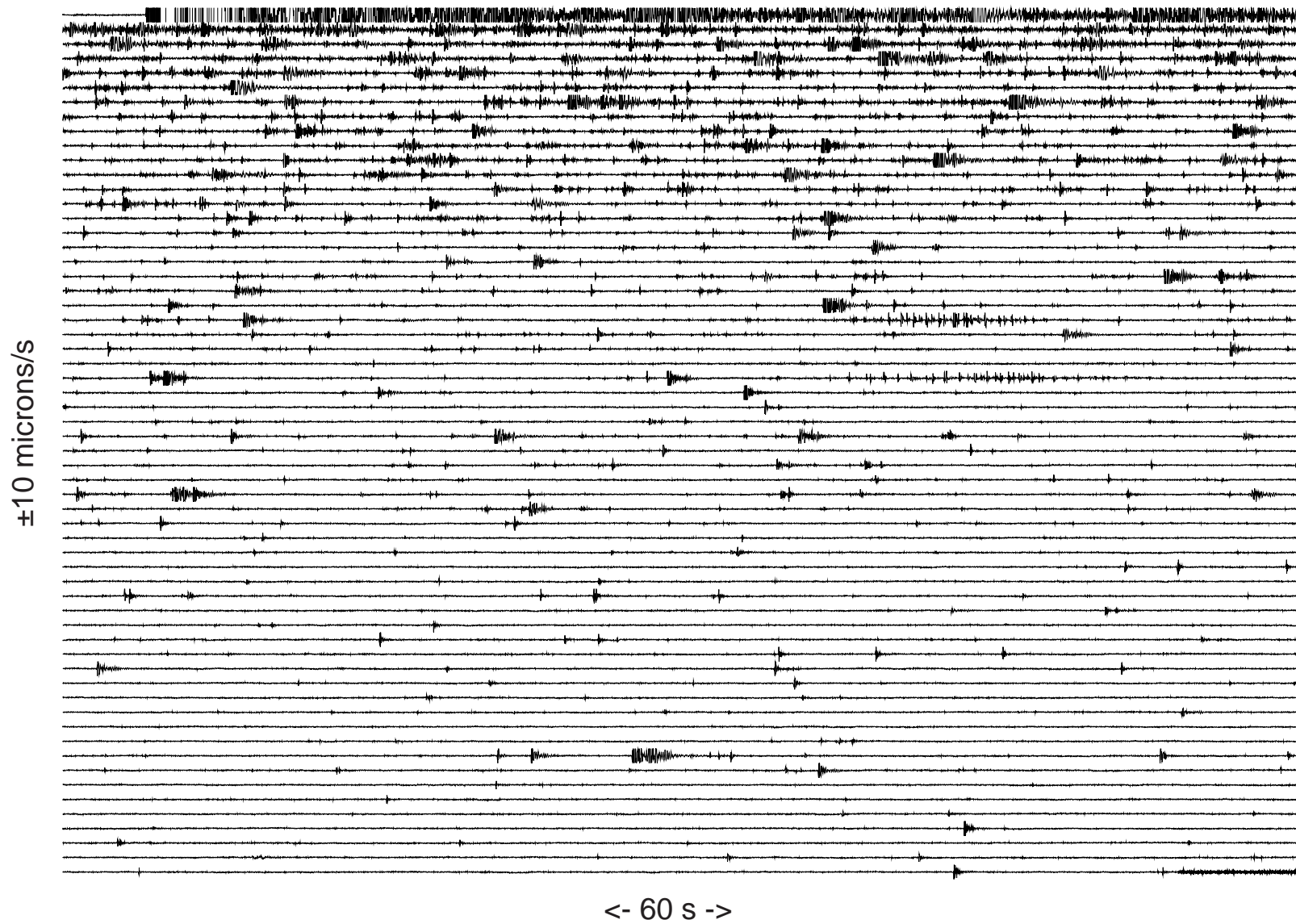


Figure 6

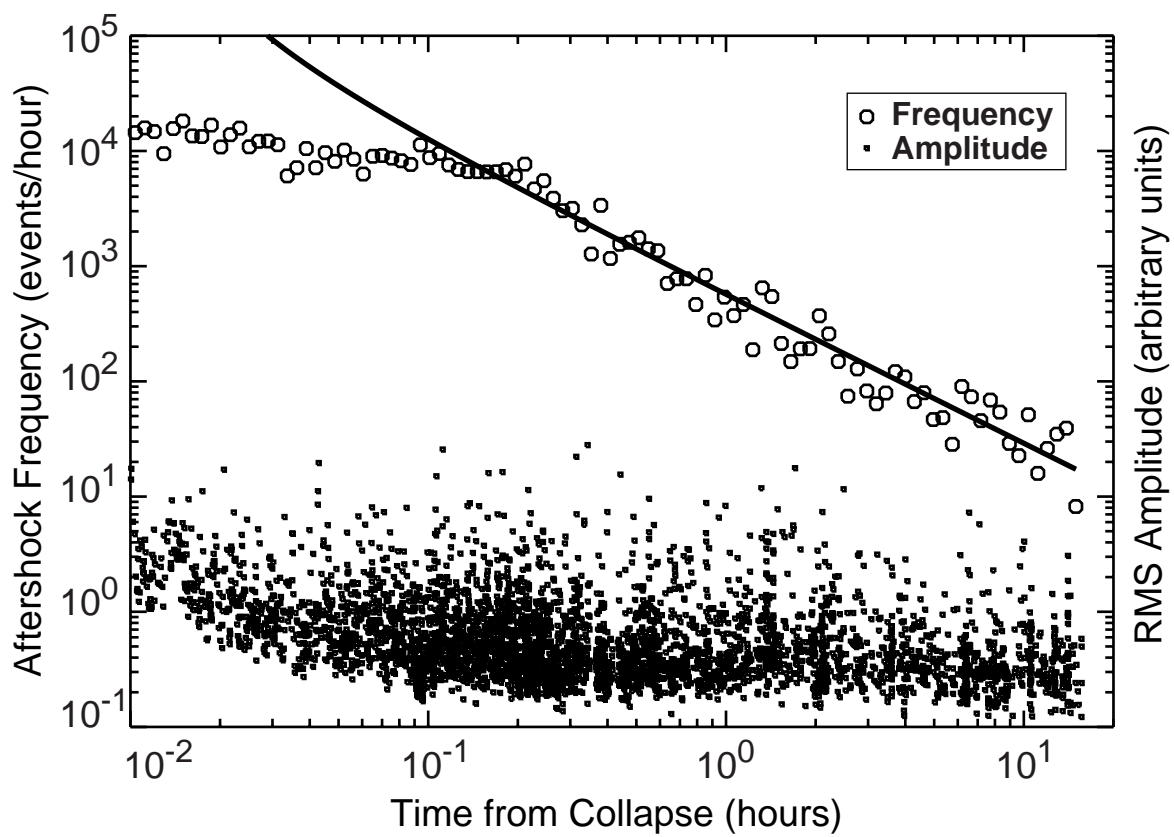


Figure 7

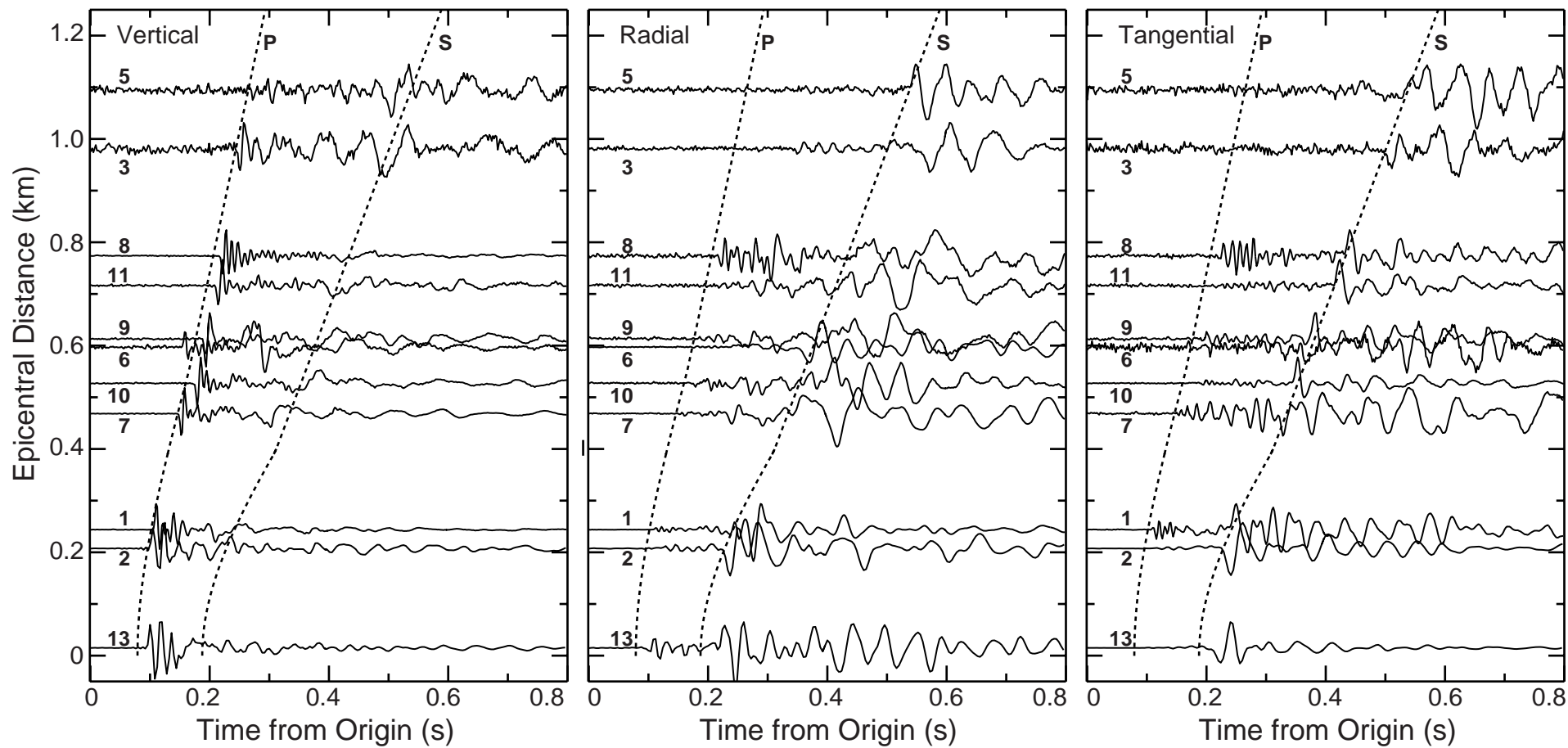


Figure 8

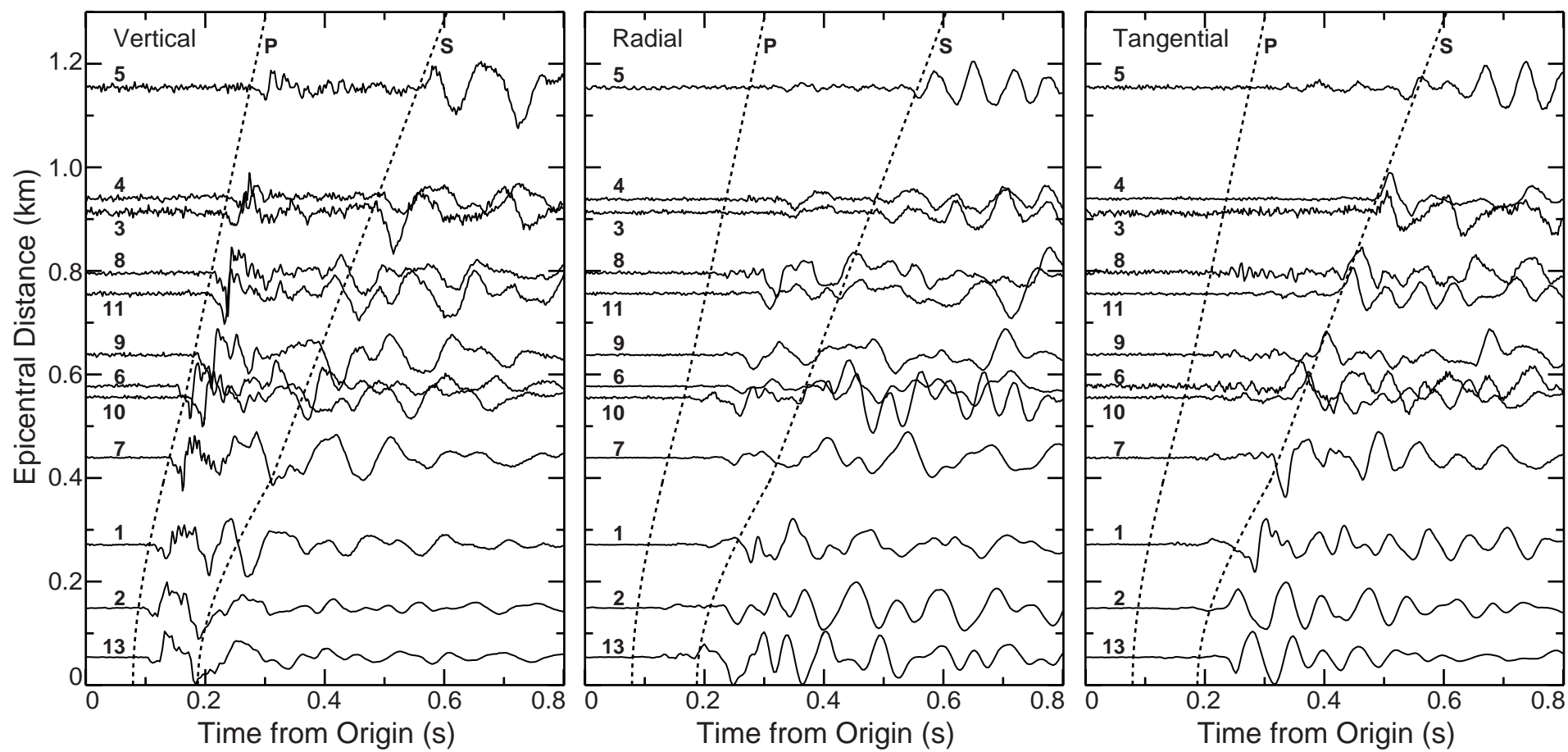


Figure 9

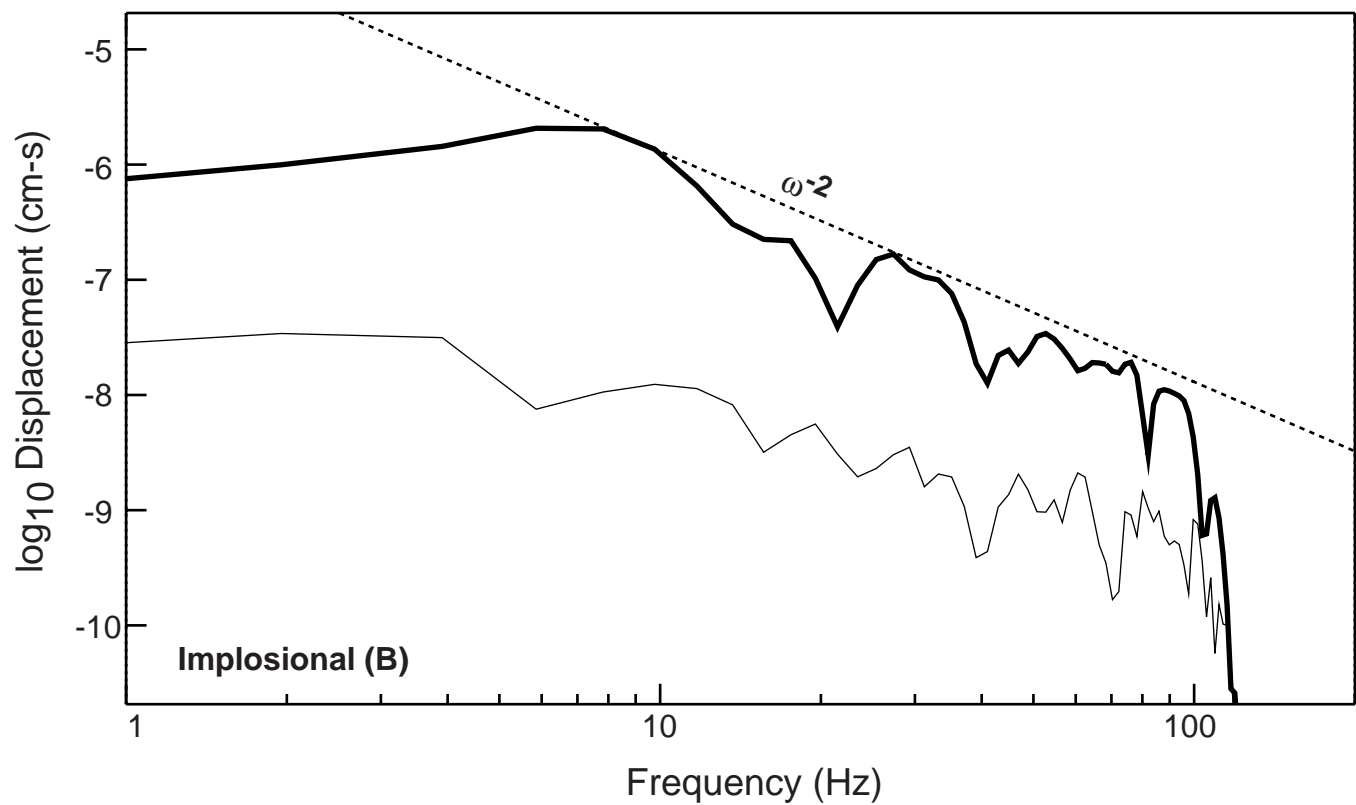
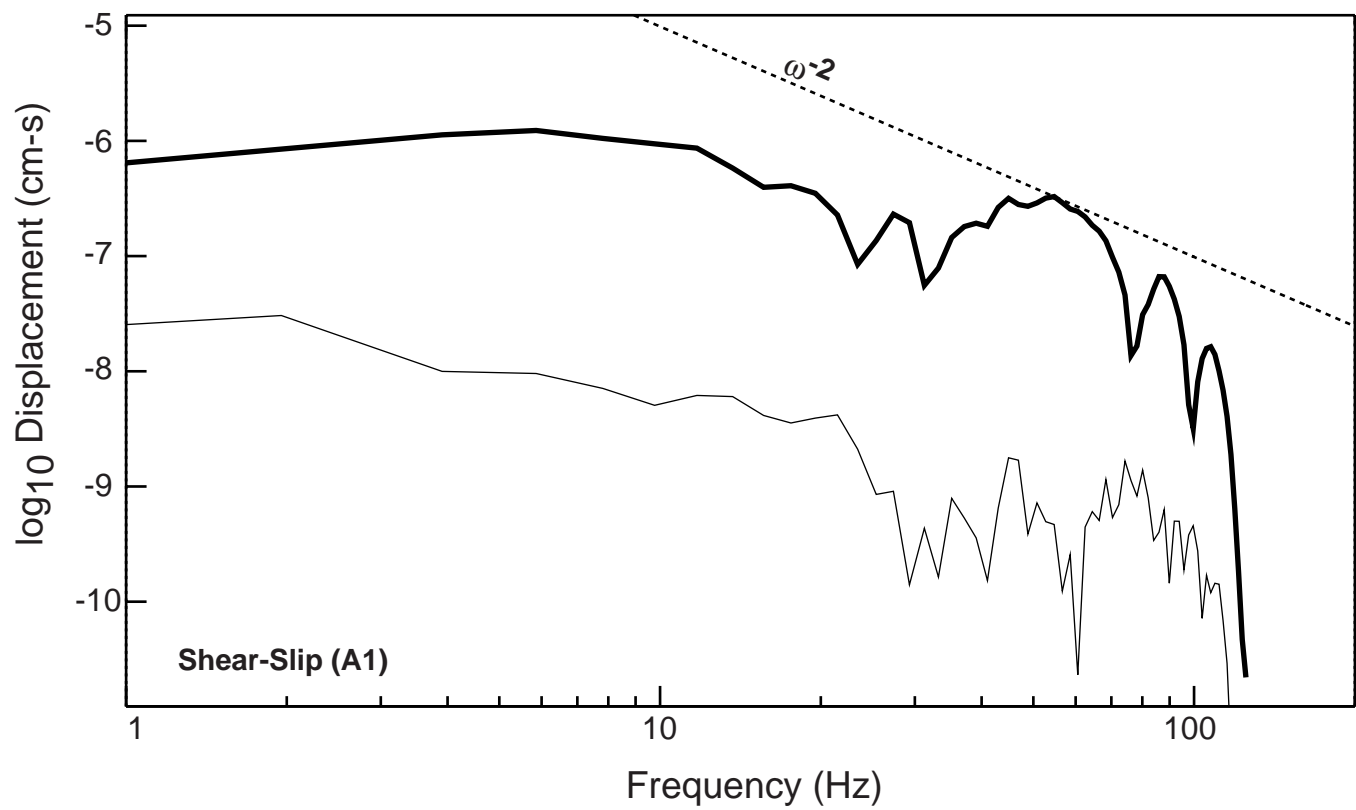


Figure 10

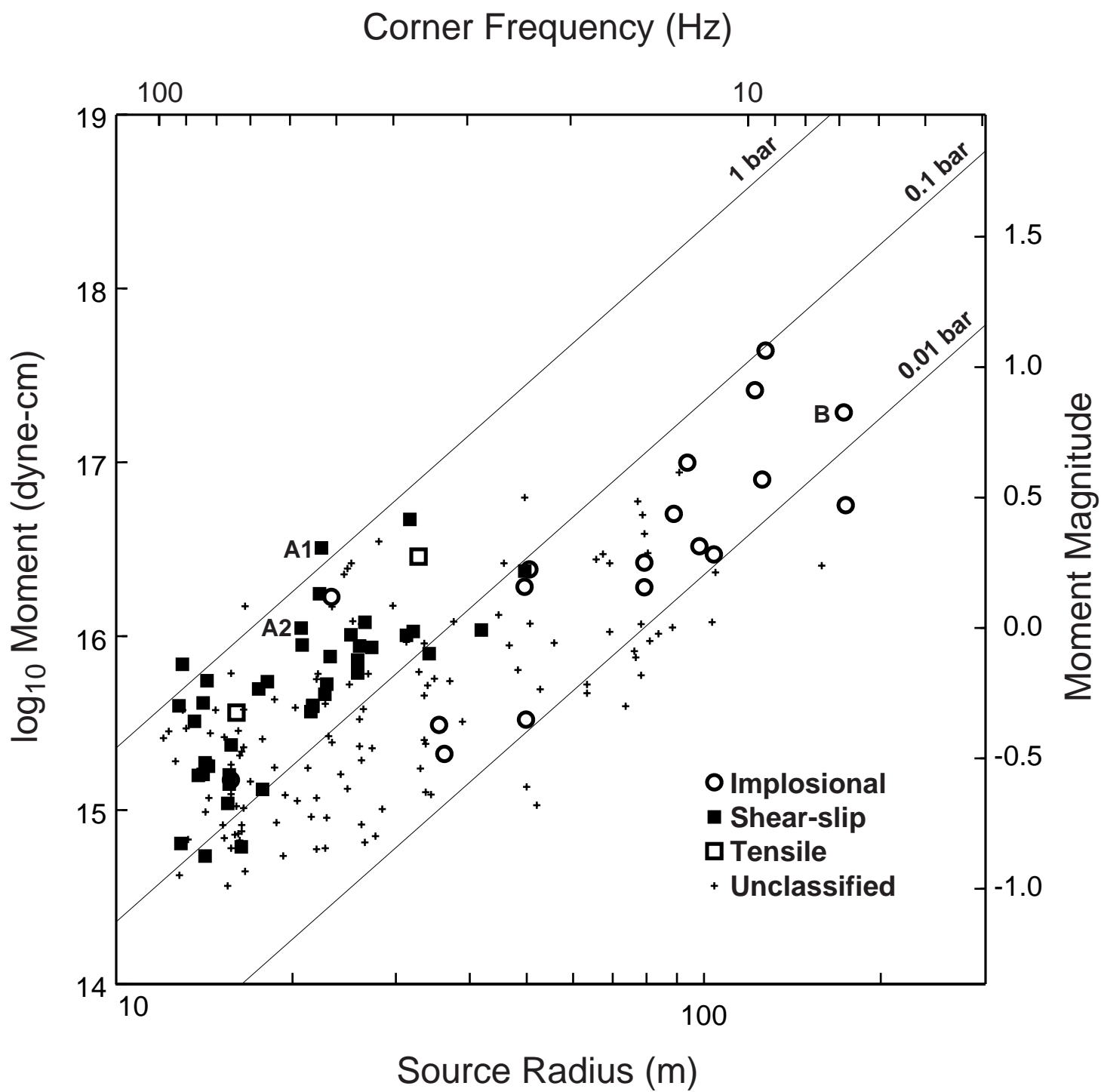


Figure 11

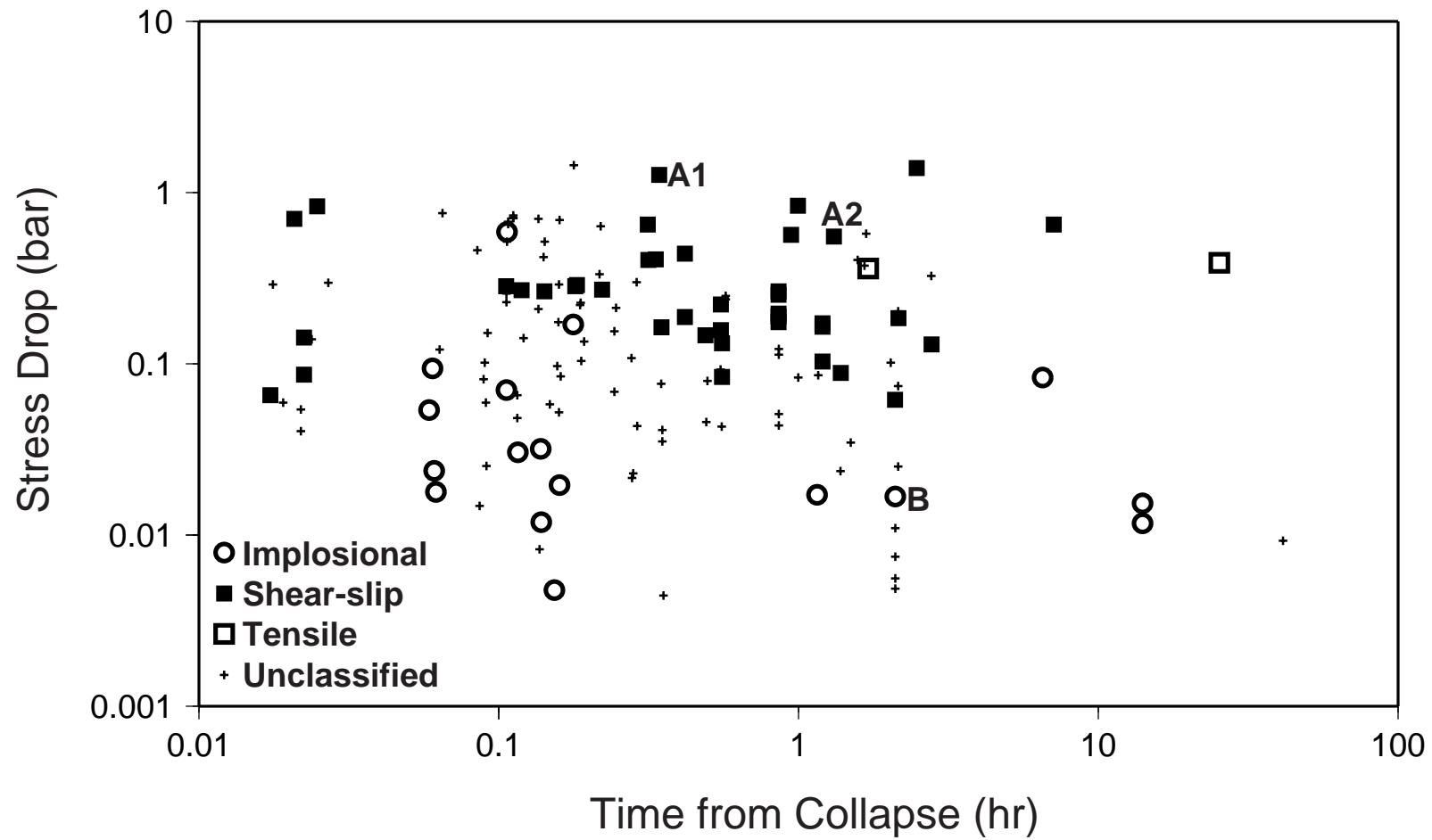


Figure 12

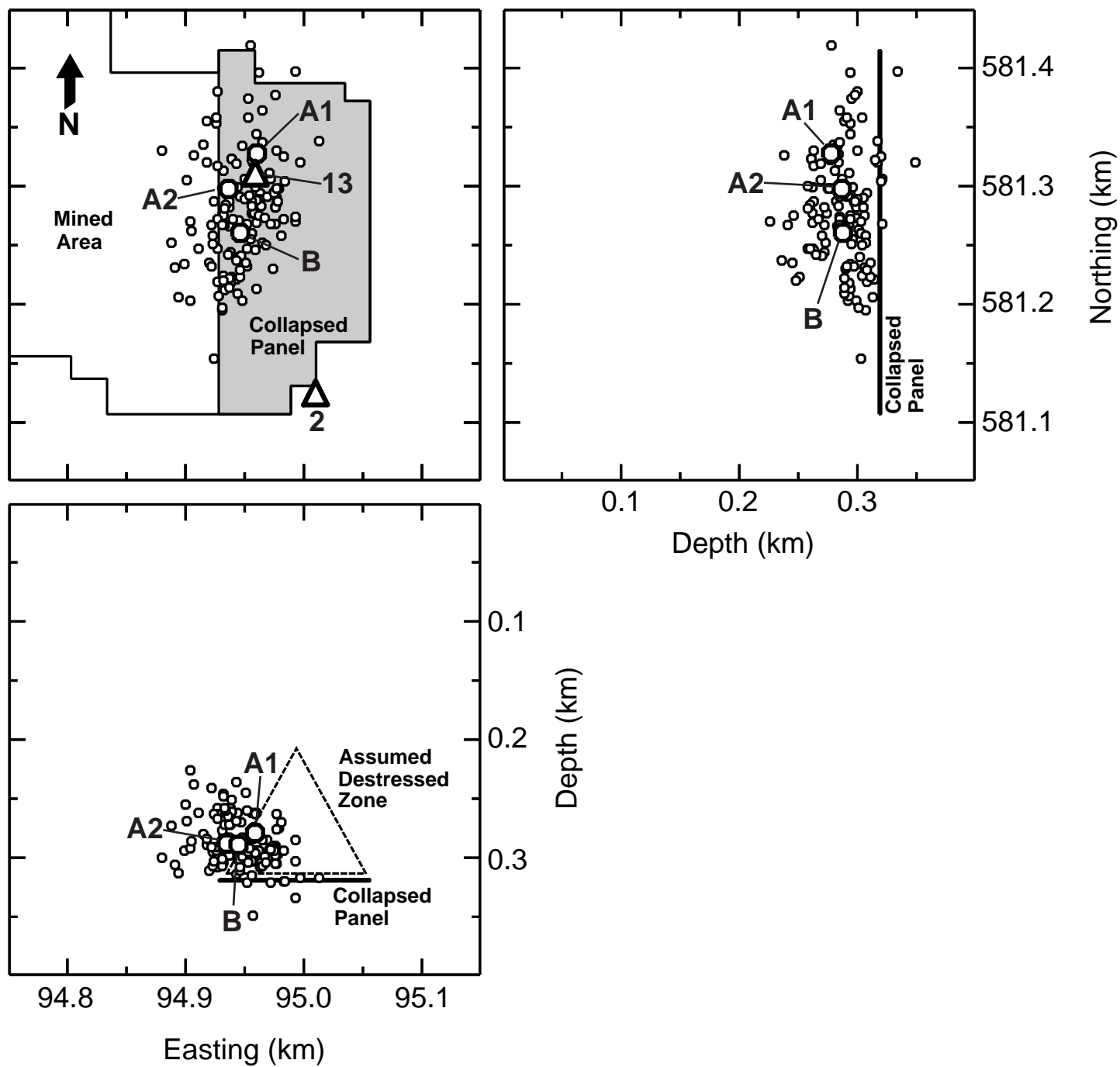


Figure 13

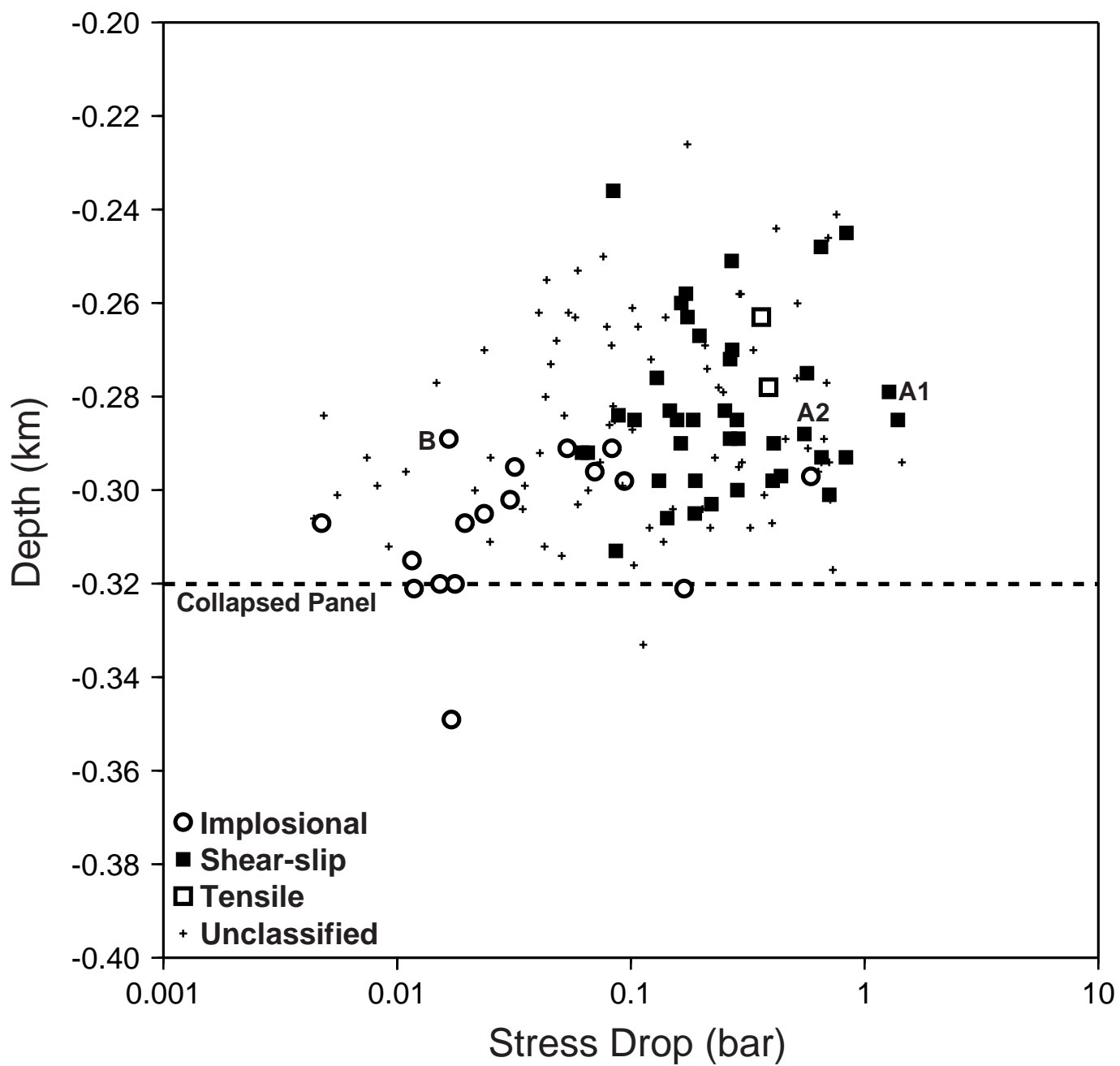


Figure 14

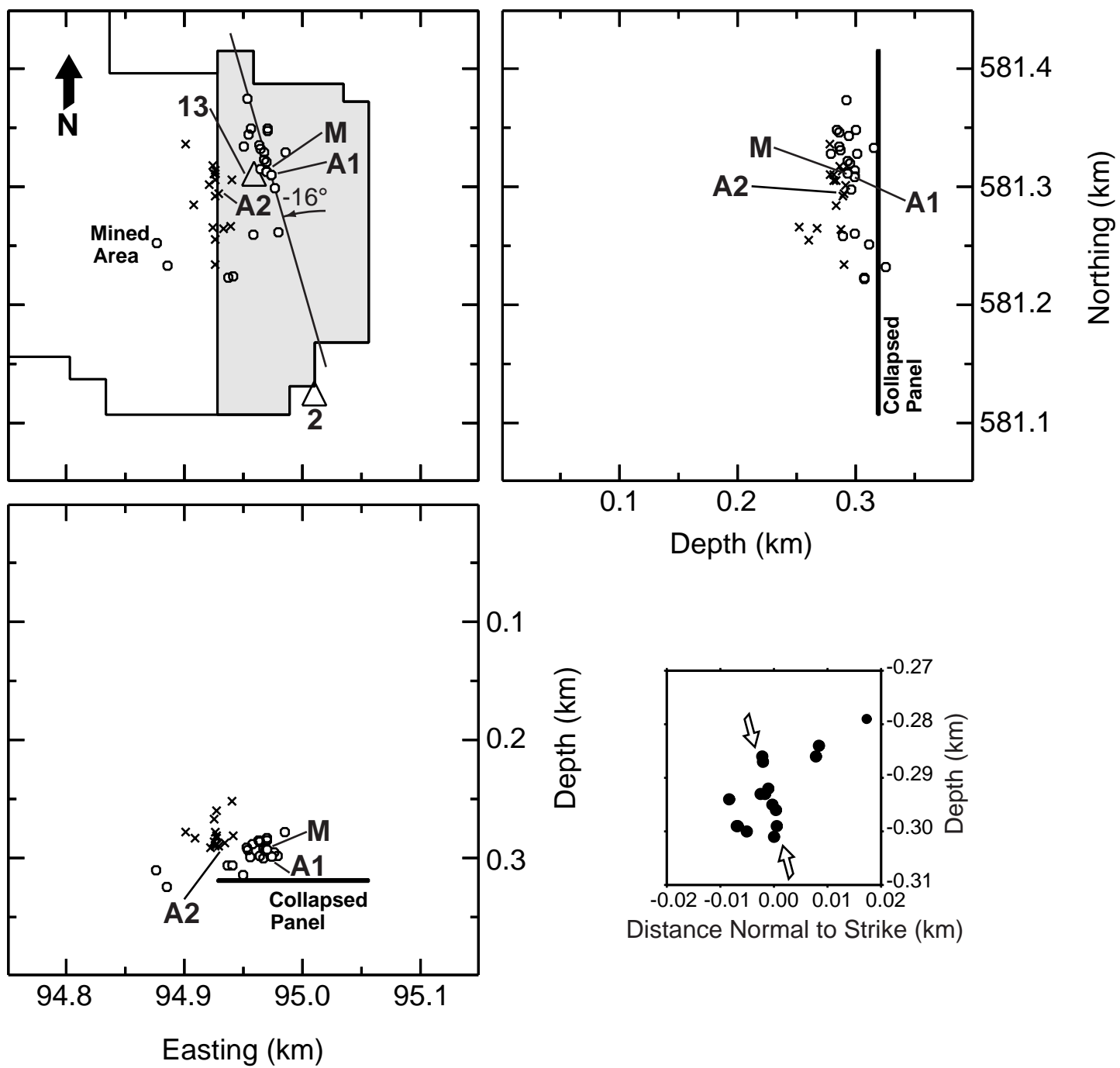


Figure 15

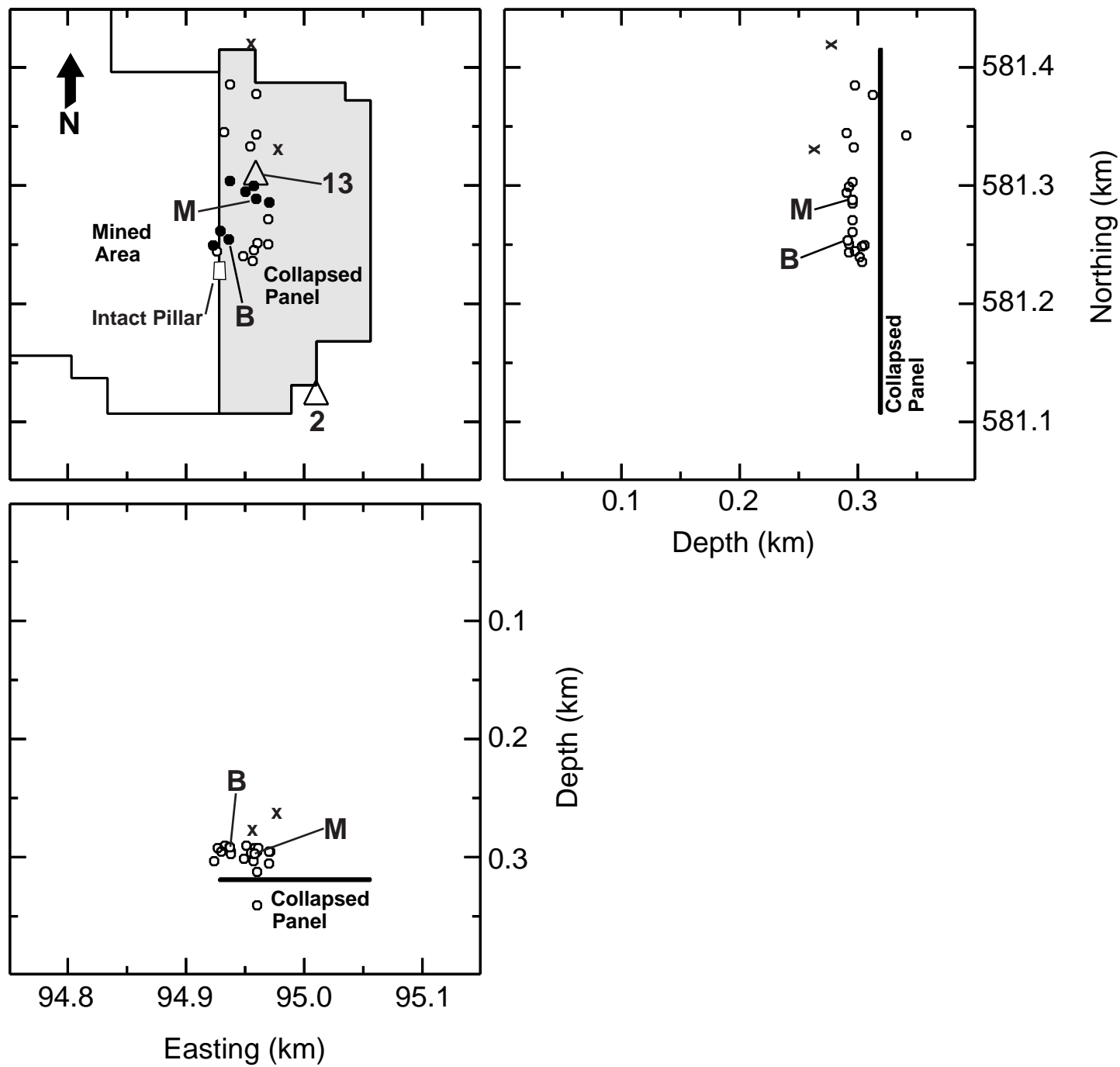


Figure 16

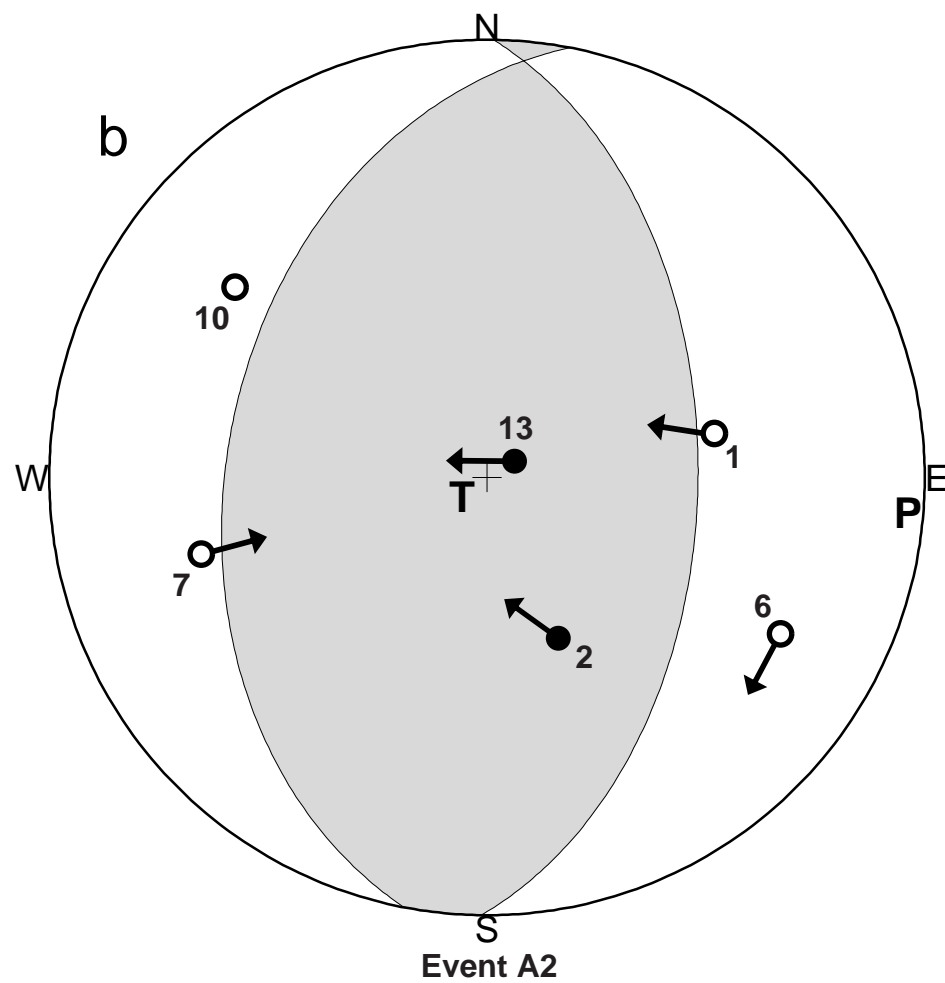
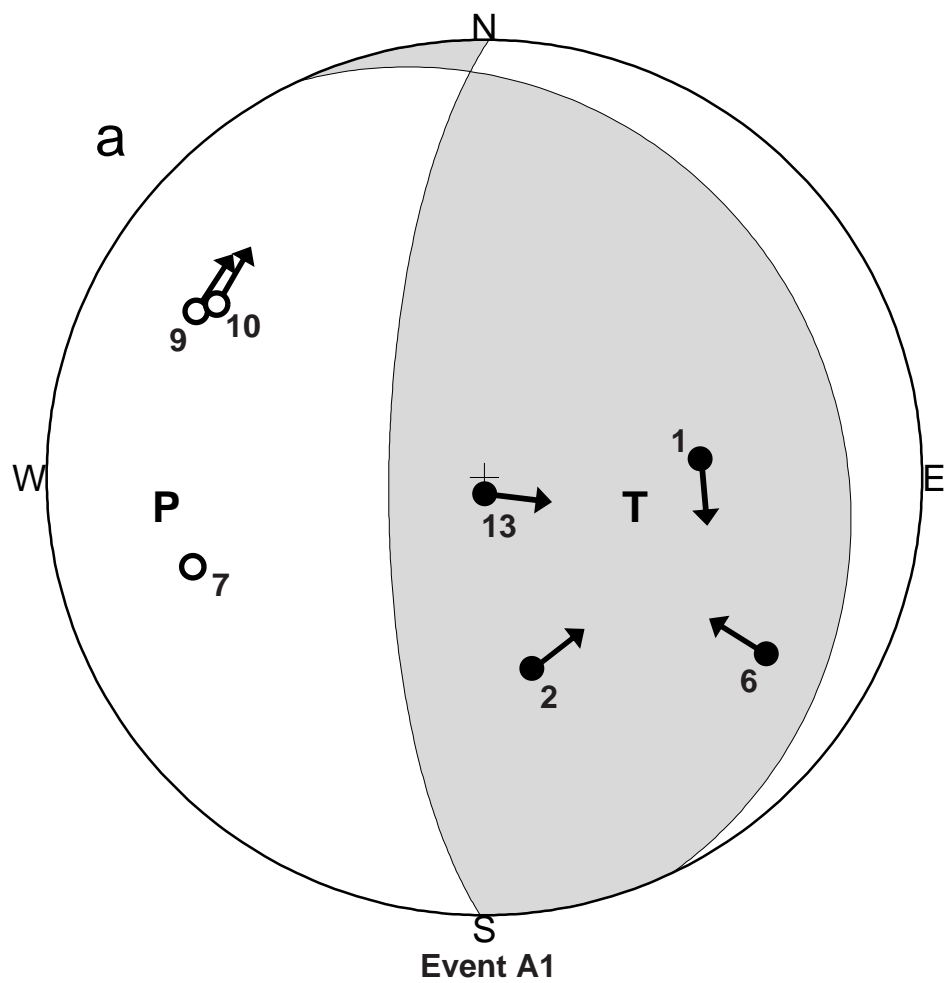


Figure 17

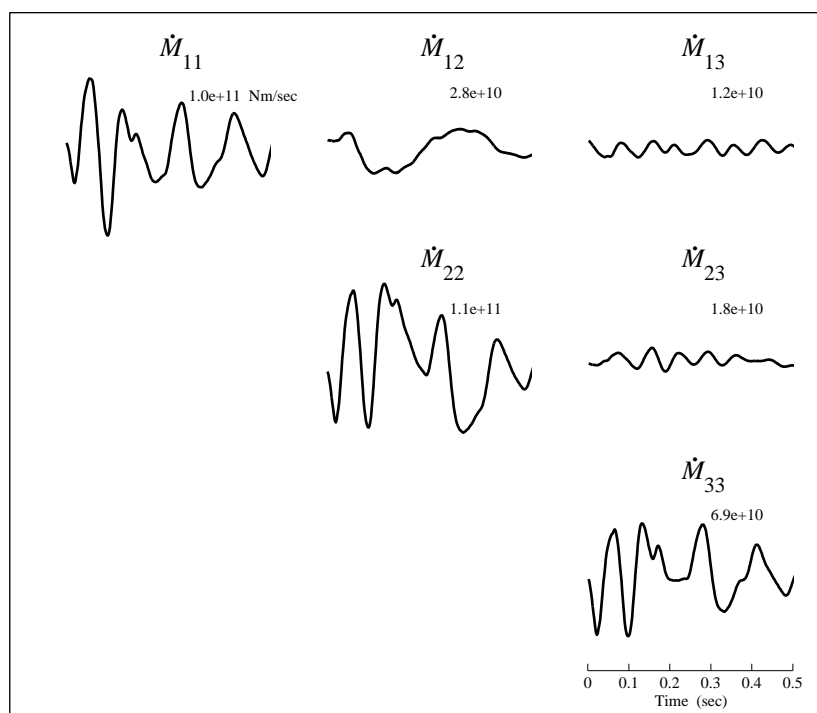


Figure 18

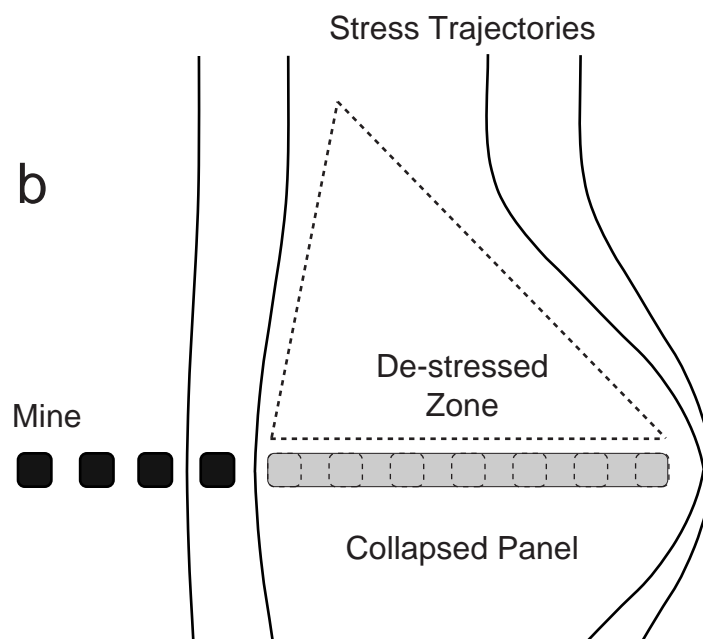
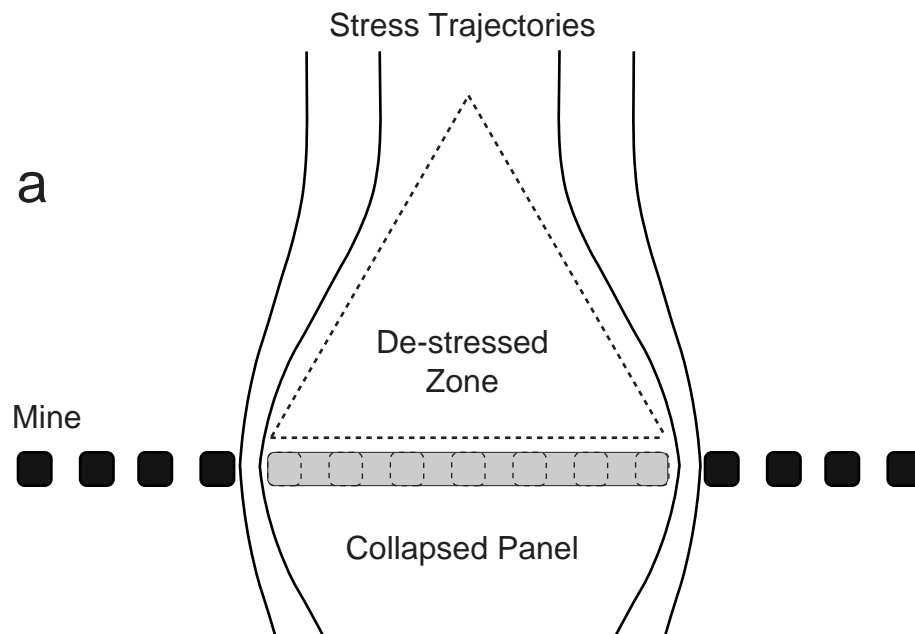


Figure 19